Accepted Manuscript

This is an Accepted Manuscript of the following article:

Influence of Suspended Sediment Front on Nutrients and Phytoplankton Dynamics off the Changjiang Estuary: A FVCOM-ERSEM Coupled Model Experiment

Jianzhong Ge[1, 2*], Ricardo Torres[3], Changsheng Chen[4], Jie Liu[5], Yi Xu[1], Richard Bellerby[1,6], Fang Shen[1], Jorn Bruggeman[3], Pingxing Ding[1]

[1]State Key Laboratory of Estuarine and Coastal Research, East China Normal University, Shanghai, China, 200062

[2]Institute of Eco-Chongming，No.20 Cuiniao Road, Chenjiazhen, Shanghai, China, 202162

[3]Marine Ecosystems Models & Predictions, Plymouth Marine Laboratory, Prospect Place, The Hoe, Plymouth, PL1 3DH, UK

[4]School for Marine Science and Technology, University of Massachusetts-Dartmouth, New Bedford, MA 02744, United States

[5]Depeartment of Biological Sciences, University of Bergen, Postbox 7803, N- 5020, Bergen, Norway

[6]Norwegian Institute for Water Research, Thormølensgate 53D, N-5006, Bergen, Norway

Corresponding author: Dr. Jianzhong Ge (jzge@sklec.ecnu.edu.cn)

Abstract

High-turbidity water is a common feature in the estuary and inner shelf. Sediment suspension functions as a modulator that directly influences the interactions among nutrients, phytoplankton and other related ecosystem variables. A physical-biological coupling model system was applied to examine the impact of sediment front on interactions among on suspended sediment, vertical mixing, nutrients and phytoplankton over the inner shelf off the high-turbidity, phosphate-limited Changjiang Estuary. The physical model was the Finite-Volume Community Ocean Model (FVCOM) and the biological model was the European Regional Seas Ecosystem Model (ERSEM). Results revealed that in the nearshore region the growth of phytoplankton over the spring-summer seasons was limited by suspended sediments and intensified vertical mixing during the autumn-winter seasons extended the sediment-induced suppression extended offshore to restrict the phytoplankton growth over the shelf. Nutrients were diluted by spreading of freshwater discharge and significantly decreased off the suspended sediment front due to the depletion by the offshore phytoplankton growth. The simulation results showed that although the diatom phytoplankton dominated the Chlorophyll a (*Chl-a*) concentration, the non-diatom group had a more contribution to the biomass. The relatively high phytoplankton biomass was found over the offshore deep underwater valley area as results of remote advection by the Taiwan Warm Current and weak turbulent mixing.

1 Introduction

Estuaries are highly productive system in which physical, biogeochemical and ecological processes strongly interact. Dissolved and particulate matters (organic and inorganic), including nitrogen (N), phosphorus (P), silicon (Si) and carbon (C), enter the estuary through upstream rivers, point discharges from human wastewater, and non-point fluxes from the land along the coast as well as submarine groundwaters (Sadat-Noori, et al., 2016; Moore, 2006, 2010). In an estuary, the growth of phytoplankton is controlled by the abiotic and biotic components in the nutrient cycles of the ecosystem (Klausmeier et al., 2008). Nutrient loadings from various sources make an estuary become a nutrient-rich ecosystem, where abundant supplies of nutrients greatly impact biological productivity.

Suspended sediment is a common feature in estuaries. In a high-turbidity region, sediment resuspension has a great impact on nutrient cycles and phytoplankton community (Kang et al., 2013; Franklin et al., 2018). On the biological level, resuspension activates the nutrient exchange between the water column and bottom benthic layer, and hence enhances the non-diatom plankton growth in the water column (Chen et al, 2004; Boynton et al., 2018). On a physical level, suspended particulate sediments reduce light penetration in the water column. In a high-turbidity environment, the phytoplankton growth is light limited. Increasing light attenuation coefficient limit the photosynthesis process and thus primary production in a nutrient-rich region (Ji et al., 2002; Chen et al., 2004; Vanderploeg et al., 2007; Donohue and Molinos, 2009; Sobolev et al., 2009; Huettel et al., 2014; Hu, et al., 2016; He et al., 2017; Niemistö, et al., 2018).

Previous observational and modeling studies have already confirmed the inhibition of suspended sediment on phytoplankton growth in the suspended sediment plume in the Changjiang Estuary (Zhu et al., 2009; Wang et al., 2019). In this estuary, however, a sediment

plume usually co-occurs with a dissolved nutrient plume as well as a low-salinity plume (Chen et al. 2003b; Ge et al, 2015). The sediment and dissolved nutrient plumes are located near the river mouth, whereas the low-salinity plume extends offshore over the shelf. Driven mainly by sediment loading and freshwater discharge in the upstream river, the sediment plume exhibits large temporal and spatial changes (Ge et al., 2015, 2018), so that the transition between suspended sediment/dissolved nutrient and low-salinity plumes varies significantly with time and in space. In this multi-plume estuarine system, the plankton dynamics are much complex, which are manifested through the fully nonlinear interaction of physical, biological and chemical processes under varying suspended sediment environment (May et al., 2003; Barbosa et al., 2010; Shi et al., 2017). Field campaigns with few sampling sites and over a short time coverage are unable to resolve the fine structures of physical and biogeochemical components, especially within the frontal zones. Some simplified numerical models were developed to simulate the phytoplankton growth and nutrient cycles in turbid estuaries (May et al., 2003; de Swart et al., 2009). These models, however, usually failed to resolve the short-term highly-varying temporal and spatial scales, which integrate to form the mid- and long-term variability of the pelagic planktonic ecosystem. Assessing the impact of sediment plume on the ecosystem in a high-turbidity estuarine environment requires an integrated three-dimensional numerical model capable of comprehensively capturing the interactions between sediment and biogeochemical processes, which was demonstrated by previous modeling studies in Great Lakes (Ji et al., 2002; Chen et al., 2004), but was scarce in estuaries. Since sediment resuspension in the high-turbidity estuaries is highly controlled by tidal currents regulating with winds and waves, the leading physical drivers, such as tides, waves and dominant estuarine and costal currents, must be integrated into the model.

In this study, we applied a fully physical and biogeochemical coupled model to examine the impact of sediment plume on the variability of nutrients and phytoplankton in the mega turbid and eutrophic Changjiang (Yangtze) Estuary and inner shelf of the East China Sea (ECS). One novelty of this study is to highlight the development of a realistic, comprehensive biogeochemical model system consisting of the interaction among surface waves, sediments, tides, coastal/oceanic currents over finer temporal and spatial scales. The other novelty lies in the exploration of ecosystem responses to high nutrient loading in a high-turbidity estuarine environment.

This paper is organized as follows. In Section 2, the study area and massive collection of observational data in the Changjiang Estuary and adjacent inner shelf of the ECS are introduced, following with the description of the coupled physical and biogeochemical model. In Section 3, the validation results of the model via observational data are presented. In Section 4, the effect of the sediment plume on the offshore nutrient and phytoplankton dynamics is evaluated. In Section 5, the dynamics controlling the physical-and-biogeochemical interaction in the Changjiang Estuary and inner shelf of ECS are discussed. Finally, in Section 6, major findings are summarized and conclusions are drawn.

2. Study area, data and model

2.1 Study area

The region of the Changjiang Estuary and inner shelf of the ECS is a typical estuarine-shelf coastal zone with a large input of freshwater and sediment from the upstream river (Fig.

108 1a). Over the period of 1950-2010, the annually-averaged freshwater volume entering this
109 estuary was ~896 km^3, with a sediment load of ~390 Mt (CWRC, 2011). The freshwater
110 discharge and sediment loading were measured at the Datong hydrological station locating ~620
111 km upstream from the ECS. This station is considered as a boundary site between the river and
112 estuary. The freshwater discharge varies significantly with seasons. The average freshwater
113 discharge is ~40 km^3/s in the wet season and ~13 km^3/s in the dry season (Luan et al., 2016).
114 Mixing of freshwater with the oceanic water forms a low-salinity plume. This plume changes
115 seasonally in terms of its spreading areas and pathway, flowing either into the ECS shelf during
116 summer or further away along the Zhejiang coast during winter (Chen et al., 1994; Ge et al.,
117 2015b). In summer, the large freshwater discharge makes the low-salinity plume enter the ESC
118 shelf region, where it interacts with the large-scale regional oceanic circulations, such as the
119 Yellow Sea Coastal Current (YSCC), the intrusion of Taiwan Warm Current (TWC, a sub-
120 stream of the Kuroshio Current) and even Kuroshio (Chen et al., 1994 and 2008) (Fig. 1a).

121
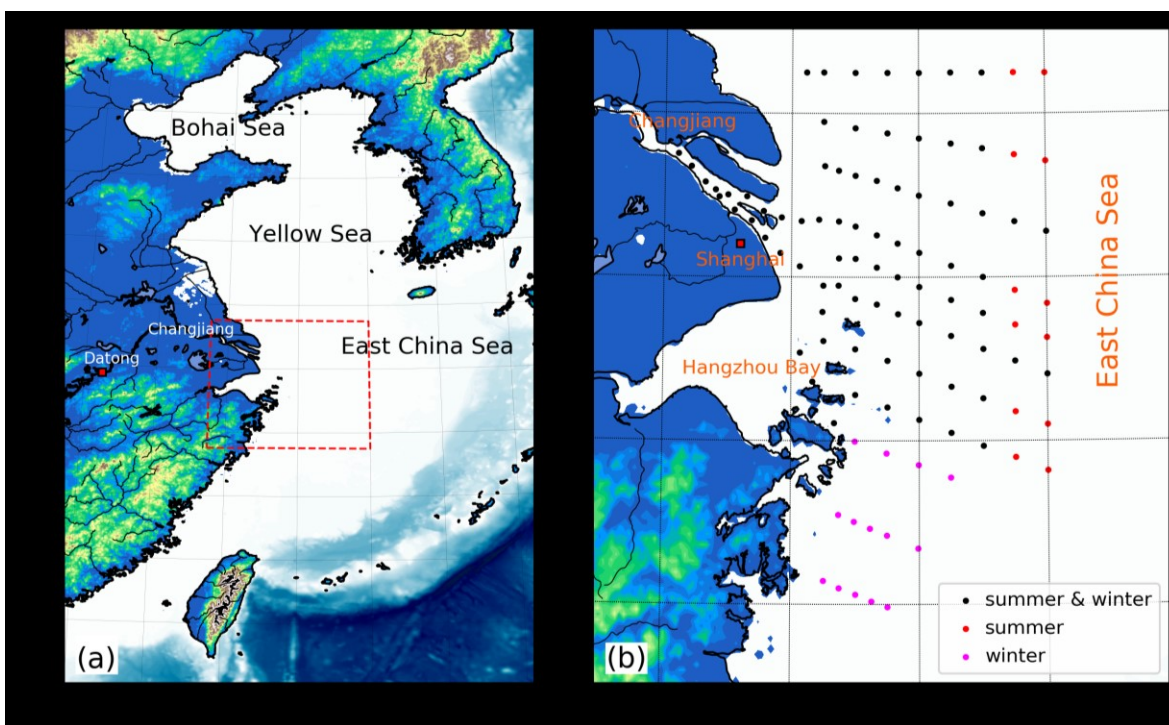
Figure 1. The locations of the Changjiang River, the Datong hydrological station and the East China Sea (a). The
panel (b) is an enlarged view of the area bounded by the dashed rectangle in panel (a). The pink and red dots
indicate the survey sites taken in winter and summer, respectively. The black dots indicate the survey sites taken in
both winter and summer.

126 The abundant sediment loading from the upstream Changjiang River makes this estuary
127 and its adjacent inner shelf of the ECS become a high-turbidity environment. The high-turbidity
128 are clearly appeared in remote sensing images and measured in the field surveys (Siswanto et al.,
129 2011; Sokolowski et al., 2014; Ge et al., 2015). The suspended sediment concentration varied
130 significantly with time and in space, with a range of ~0.1-1.0 g/L near the surface inside the
131 estuary and of < 0.2 g/L in the offshore region (Ge et al., 2015).

132 In the recent years, with the rapid economic growth and corresponding increase in
133 fertilizer use in agriculture, the Changjiang Estuary has experienced a dramatic increase period in

134 nutrient loading. The environmental monitoring recorded at the Datong station from 1960 to
135 2000 indicated a sharp rise in nutrients, with the concentration of dissolved inorganic nitrogen
136 (DIN) and phosphate (DIP) increasing from ~20 μmol/l to ~130 μmol/l, and from ~0.2 μmol/l to
137 ~1.6 μmol/l, respectively (Li et al., 2007). This evidence was also reported early by Chen et al.
138 (2003b) based on other data sources. In contrary to DIN and DIP, however, the dissolved
139 inorganic silicate (DSi) dropped from ~120 μmol/l to ~70 μmol/l, resulting from fixation of DSi
140 within hundreds of reservoirs built along the Changjiang river (Friedl and Wüest, 2002;). These
141 nutrient changes have caused severe eutrophication problems in the area and a dramatic change
142 in the ratio of N: Si in the Changjiang Estuary and inner shelf (Zhou et al., 2008; Jiang et al.,
143 2010; Zhu et al., 2014; Zhou et al., 2017).

144   Under a nutrient-rich environment, the high primary production and phytoplankton
145 bloom were often observed in the Changjiang Estuary and it adjacent inner shelf of the ECS
146 (Furuya et al., 1996， 2003), with a Chlorophyll-a (*Chl-a*) concentration of >10 μg L^{-1} off the
147 (Chen et al., 2003b; Zhu et al., 2009) and even reached ~20 μg L^{-1} when the harmful algal bloom
148 occurred (Chen et al., 2003b). The diatom remains to be a predominant species contributing to
149 the total phytoplankton *Chl-a* (>90%). Recent surveys reported that dinoflagellates have become
150 dominant component in the phytoplankton community, particularly in the high resuspended
151 sediment plume (Chen et al., 2003b) and in eutrophic onshore waters influenced by the low-
152 salinity plume (Jiang et al., 2015).

153   2.2 The cruise data

154   Massive physical and biogeochemical data were collected from multiple field campaigns.
155 Observational sites covered the river channel, estuary and inner shelf of the ECS (Fig. 1b).
156 Responding to different patterns of Changjiang River plume's extensions in summer and winter
157 around the inner shelf, 14 more sampling sites were placed in the south of the Changjiang
158 Estuary during winter plus additional 12 sites in the east of the inner shelf in summer (Fig. 1b). A
159 total of 90 and 92 sites were visited during the summer and winter cruises, respectively. Physical
160 and biogeochemical variables were measured at these sites. The physical variables contained
161 water velocities from a vessel-mounted Acoustic Doppler Current Profiler (ADCP), temperature
162 and salinity from sensors of Conductivity-Temperature-Depth (CTD). The biogeochemical
163 variables included pH, nutrients including DIN, DIP, ammonia (NH4), and DSi, *Chl-a*, and
164 suspended particulate matter (SPM). Cruises periods covered every winter and summer over the
165 period of 2015 to 2017.

166   2.3 The satellite data

167   Both surface sediment concentration and phytoplankton *Chl-a* can be calculated from
168 satellite remote sensing data (O'Reilly et al., 1998; Shen et al., 2010). In this study the satellite
169 data were used for model validation and interpretation. The data came from two sources. One
170 was the 4-km-resolution-mapped daily *Chl-a* field from Moderate Resolution Imaging
171 Spectroradiometer Aqua satellite (MODIS-Aqua, https://oceancolor.gsfc.nasa.gov/data/aqua/),
172 which covered the period from January 1 2005 to December 31 2016. The other one was the 500-
173 m-resolution-mapped hourly sky-view observational data from the Multi-channel Geostationary
174 Ocean Color Imager (GOCI) satellite, which covered the East Asian seas and recorded every 8
175 hours per day (Cho et al., 2012, 2014). Surface *Chl-a* concentrations were retrieved and
176 calculated using the ocean chlorophyll 2 algorithm (OC2) (O'Reilly et al., 1998; Ryu et al., 2012)

177 through the GOCI Data Processing System (GDPS version 1.4.1) from 2012 to 2016, in which
178 the Korea Ocean Satellite Center (KOSC) standard was applied in atmospheric correction. For
179 public access, the daily product contained three snapshots taking at 10:30 am, 11:30 am and
180 12:30 am, respectively.

181 Generally, in coastal optically complex waters, *Chl-a* algorithms suffer from the
182 contamination by colored particulate and dissolved substances. Using the semi-empirical
183 radiative transfer (SERT) algorithm with physical based empirical coefficients (Shen et al.,
184 2010), the GOCI optical reflectance data were used to estimate surface sediment concentrations
185 in the Changjiang Estuary (Choi et al., 2012; He et al., 2013; Ge et al., 2015b), as well as *Chl-a*
186 (Choi et al., 2014; Piwowarczyk et al., 2016; Sun et al., 2018). Previous studies have already
187 confirmed the reliability of GOCI production for the *Chl-a* under the interference of colored
188 dissolved organic matters (Lamquin et al., 2012; Hu et al., 2012).

189 2.4 Hydrodynamic model

190 Main hydrodynamic forcings and components in the Changjiang Estuary include the
191 astronomical tide, river discharge, wind, waves, coastal/oceanic currents, and the sediment. The
192 core system of the physical numerical model is the Finite-Volume Community Ocean Model
193 (FVCOM). FVCOM is an unstructured-grid community ocean model, in which governed
194 equations were discretized and solved using the finite-volume integration algorithm (Chen et al.,
195 2003a) and gradually upgraded to include multiple hydrodynamic and ecosystem modules (Chen
196 et al., 2013). The non-overlapping triangular grid configured in FVCOM provided accurate
197 geometrical fitting for irregular coastlines while guaranteeing flexibility for refining the grid in
198 steep bathymetry, islands, or regions of interest (Chen et al, 2003a, Chen et al, 2006, Qi, et al.,
199 2018). An accurate finite-volume second-order Ruge-Kutta algorithm guaranteed volume and
200 mass conservations of the momentum fluxes over each iteration. Horizontal diffusion was
201 parameterized based on Smagorinsky's formation (Smagorinsky, 1963) and vertical turbulent
202 mixing was calculated using the 2.5-level Mellor and Yamada turbulence model (Chen et al.,
203 2013).

204 FVCOM is a fully current-wave coupled model (Chen et al., 2013). An unstructured-grid
205 version of the surface wave model-SWAN was developed on the platform of FVCOM and
206 named "FVCOM-SWAVE" (Qi et al., 2009). The FVCOM-SWAVE implemented to FVCOM as
207 a wave module and coupled with hydrodynamic component of FVCOM. This coupled model
208 been applied for the coastal wave and inundation applications with inclusion of wave-current
209 interactions (Wu et al., 2010; Ge et al., 2013; Beardsley et al., 2013; Chen et al, 2013; Qi et al.,
210 2018).

211 FVCOM also has incorporated a sediment module, covering from suspended sediment, to
212 bed-load transport and layered bed-soil dynamics (Chen et al., 2006). This model has the ability
213 of supporting unlimited sediment classes for non-cohesive and cohesive sediment dynamics.
214 Additionally. the wave and sediment have been fully coupled with the hydrodynamic kernel with
215 their physical interactions (Wu et al., 2010; Ge et al., 2018). The two-way coupling was
216 considered in this modeling. This means individual process (such as waves) can impact on the
217 other two processes (e.g. current and sediment).

2.5 Biogeochemical Model

The biogeochemistry and ecosystem dynamics are simulated by the European Regional Seas Ecosystem Model (ERSEM ver. 15.06), which is a generic and well established lower-trophic level marine food web and biogeochemical cycling model (Butenschön et al., 2016). It resolves the ecosystem dynamics with nutrients and carbon cycles in the low trophic levels. It divides the phytoplankton, zooplankton and benthos into function groups, and calculates the biomass for the group individually. The model calculates various state variables, including pelagic and benthic living organisms, dissolved and particulate nutrients, dissolved oxygen and carbonates. ERSEM considers the functional groups following the lower trophic food-web chain from primary producers of phytoplankton, consumers like zooplankton, to decomposers of bacteria. For phytoplankton, ERSEM could consider up to four types, according their group sizes. They include pico-, nano-, and microphytoplankton, and diatoms. ERSEM accounts for up to three types of zooplanktons in the system, from meso-, and microzooplankton and heterotrophic nanoflagellates. For decomposers, only one type of heterotrophic bacteria is considered. *Chl-a* is determined separately in the model based on the quantification formulation (Geider et al., 1997). ERSEM is also equipped with a comprehensive benthic model (Ebenhoh et al., 1995) and a fully resolved carbonate system. It provides active nutrients and mass exchanges in the water-sediment interface. The ERSEM considers both dissolved and particulate organic matter, including labile dissolved organic matter, semi-labile organic matter, semi-refractory organic matter, small particulate organic matter, medium size particulate organic matter, large particulate organic matter. The particulate organic matter for nitrogen, phosphate and silicate are all considered in autochthonous compounds, but not external/forced fluxes (Butenschön, et al., 2016). All the biogeochemical representation and mathematical formulations in ERSEM were described in detail in Butenschön et al. (2016).

3. Coupling of physical and biogeochemical models

3.1 Physical-biogeochemical model coupling

Coupling between FVCOM and ERSEM were utilized through FABM (Framework for Aquatic Biogeochemical Models; http://fabm.net) (Bruggeman and Bolding, 2014). The aim of this coupling is to provide FVCOM with a mechanism to easily incorporate new and existing biogeochemical models: FABM is a domain-independent programming framework with support for any number of processes, prognostic variables, diagnostic variables, and advanced features such as surface- and bottom layers (sea ice biota, benthos, sediment) and multiple feedbacks to physics. It comes with a comprehensive library of existing biogeochemical models, including descriptions of suspended sediment, redox chemistry (BROM) and pelagic and benthic ecosystems (NPZD, ERGOM, ERSEM).

FABM runs as part of its "host model", in this case, it is FVCOM. In a coupled FVCOM-FABM simulation, the ERSEM can be run either offline or online simultaneously with FVCOM with variable exchanges through FVCOM-FABM coupler (Bruggeman and Bolding, 2014). FABM itself provides information to biogeochemical processes, including source terms and residual vertical velocities (e.g., sinking rates) of prognostic variables, and the value of diagnostics. It doesn't handle features related to hydrodynamics or the spatial domain, e.g., transport of biogeochemical variables, surface boundary conditions (dilution/concentration due to precipitation/evaporation, open boundary conditions), rivers, reading restart files, and saving

261 output. It also doesn't manage the memory for spatially explicit fields, e.g., the physical
262 environment and the biogeochemical variables themselves. All these features are implemented in
263 the FVCOM-FABM coupler.

264   Additionally, a python-based open-source utility PyFVCOM is used to easily manipulate
265 and analyze the results from FVCOM-FABM-ERSEM simulation (Cazenave and Bedington,
266 2018).

267   3.2 Integration of model system and configuration

268   The model system for the Changjiang Estuary (Fig. 2) consisted of a shelf-scale East
269 China Sea model and coastal-estuarine scale model for the Changjiang Estuary that incorporated
270 waves and sediment dynamics. Wave-current-sediment interactions were activated only in the
271 coastal-estuarine scale model, and coupling approach was extensively described in Ge et al.
272 (2013). Differing from Ge et al. (2013), the upgraded version included the coupling of ERSEM.


273
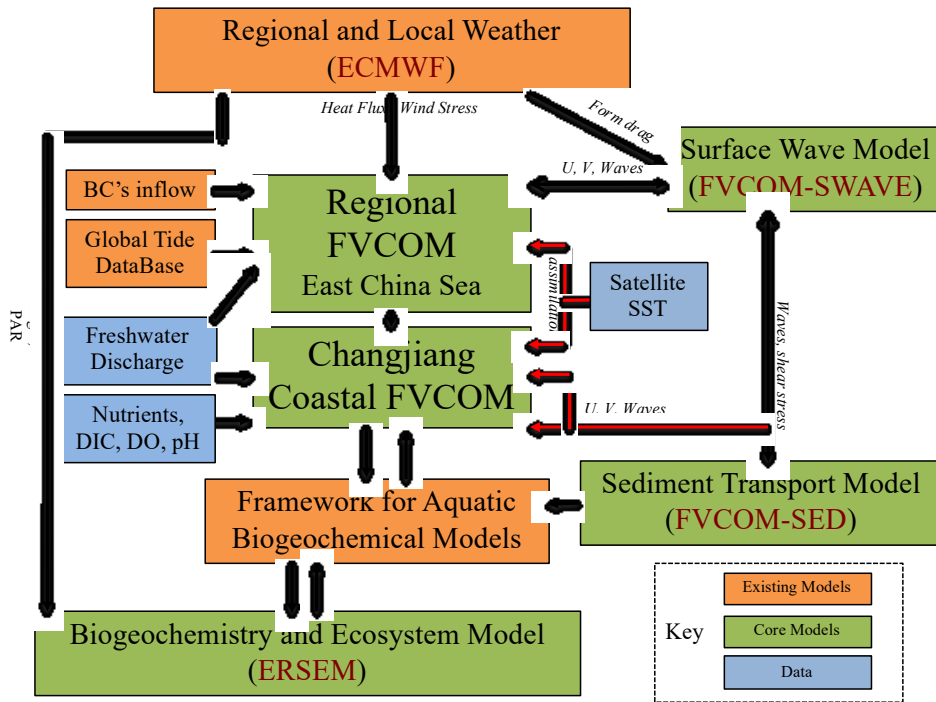
Figure 2. Framework of the FVCOM-based coupling model system for physical and biogeochemical dynamics,
including regional FVCOM model for the East China Sea and adjacent seas, coastal-estuarine FVCOM model for
the Changjiang Estuary, the surface wave model FVCOM-SWAVE, sediment model FVCOM-SED, the
biogeochemistry and ecosystem model FVCOM-ERSEM.

278   The model grids for the regional and coastal domains were shown in Fig. 3. The regional
279 model covers the adjacent shelf seas, including the Bohai Sea, Yellow Sea and the East China
280 Sea (Fig.4 a), with a mesh resolution of ~3km along the coastal region and Kuroshio path and
281 meandering region (Chen et al., 2008; Ge et al., 2013). The large domain provides the boundary
282 conditions of tide, ocean circulation and waves to the higher resolution coastal domain.

283   The coastal-estuarine domain for the Changjiang Estuary was discretized as the refined
284 mesh with a resolution of ~1-3 km in the river mouth and coastal region (Fig. 3b). The upstream

285 river boundary extended to the Datong station, which was the closest hydrological station to the
286 tidal-limit measuring runoff rate, sediment flux and biological variables' concentrations. The
287 coastal-estuarine domain covered the high-turbidity region in the estuary, including the
288 Hangzhou Bay and the Jiangsu offshore region. The lateral open boundary was placed at
289 124.5°E, while the north and south lateral boundaries were located at 34.2°N and 28.25°N,
290 respectively, with the purpose of eliminating the noise from the boundaries in our estuarine
291 region of interest.
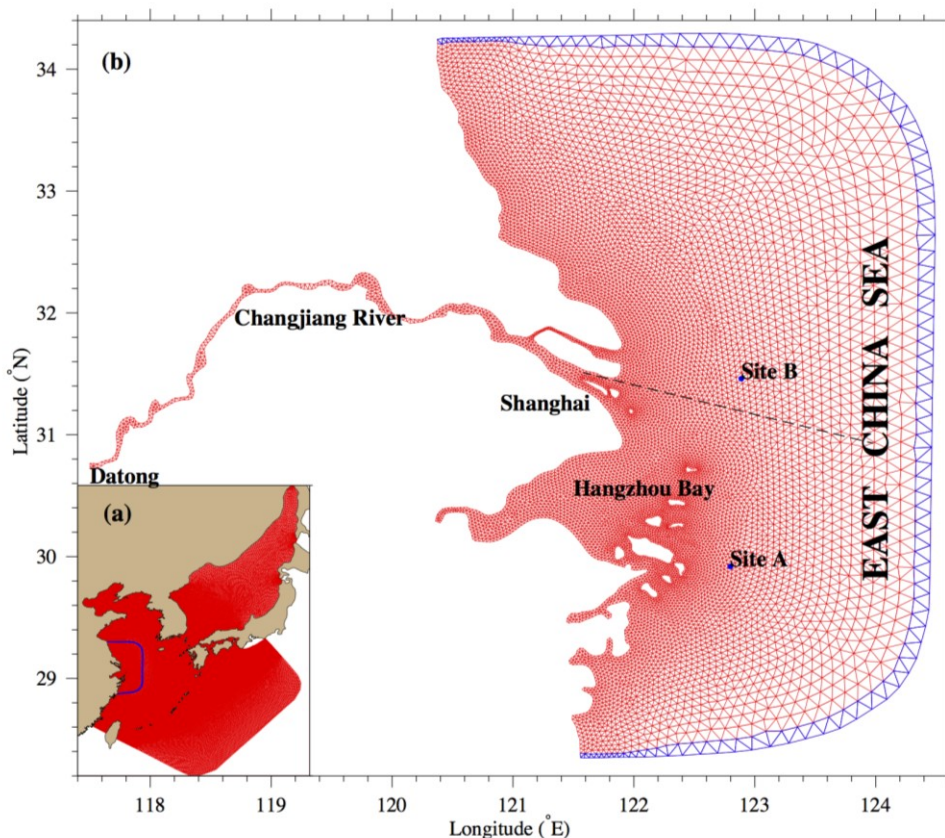
292

293 **Figure 3.** Unstructured meshes for the shelf-scale East China Sea model (a) and coastal-estuarine scale Changjiang
294 Estuary model (b). Two individual locations (Site A and B) and one section (blue dashed line) from the river mouth
295 to the offshore region are included in (b).

296 The Connecting between the regional and coastal domains was performed with a one-way
297 nesting method. These two model meshes shared a common-grid layer with identical bathymetry,
298 horizontal and vertical coordinates (blue lines in Fig. 3). This common-grid nesting method
299 guaranteed the conservation of mass and momentum during regional-to-coastal nesting (Chen et
300 al. 2013; Ge et al., 2013; Qi et al., 2018), thus this coupling of physical and biogeochemical
301 dynamics through FABM was only active in the coastal-estuarine scale domain (Fig. 2).

302 The simulation covered the period from January 1 1999 to December 31 2016. The
303 atmospheric conditions were driven by ERA Interim data from European Centre for Medium-
304 Range Weather Forecasts (ECMWF). Surface wind velocities at 10 m height, shortwave,
305 longwave, latent and sensible radiation flux were provided at a 6-hour interval. Lateral boundary
306 conditions were specified with a hybrid forcing of astronomical tide and subtidal oceanic

307 currents. The tidal boundary condition for the regional domain includes eight major tide

308 harmonic constituents, M_2, S_2, K_2, N_2, K_1, O_1, P_1, and Q_1, retrieved from TPXO 7.2 Global Tidal

309 Solution (Egbert and Erofeeva 2002). Volume transport along the lateral boundary is interpolated

310 from daily HYCOM/NCODA Global 1/12° Analysis data (GLBa0.08 branch). The upstream

311 river boundary was driven by the daily freshwater and sediment discharges collected at the

312 Datong station (www.cjh.com.cn).

313 Satellite-derived sea surface temperature (SST) data were assimilated in the model with a

314 nudging algorithm (Chen et al., 2013). Daily SST data from the Advanced Very High-Resolution

315 Radiometer (AVHRR) L4 at 0.25° resolution was assimilated in the model over the period from

316 1999 to 2004, while the data from GHRSST/JPL (https://podaac.jpl.nasa.gov/GHRSST) at

317 0.011° resolution over the period from 2005 to 2016. The wave model followed the

318 configuration described in Ge et al. (2013). The sediment model shared the same parameters as

319 Ge et al. (2015). The spatially non-uniform distribution of the critical shear stress for erosion,

320 adopted from Ge et al. (2015), were also applied in this configuration.

321 Since the main purpose of our modeling study was to examine the nutrients and

322 phytoplankton dynamics in the pelagic system and the benthic ecosystem is not a dominant

323 contributor, only the pelagic (non-benthic) dynamics were considered here.

324 To avoid zero values of the carbonate system variables at the river nodes, the dissolved

325 oxygen (DO), carbonate bio-alkalinity, total alkalinity, and carbonate total dissolved inorganic

326 carbon (DIC) were specified by constant values of 300 mmol O/m^3, 2.50 µmol/kg, 2065.0

327 µmol/kg, and 2200.0 mmol C/m^3, respectively. Nutrient concentrations at the lateral boundaries

328 were interpolated from the World Ocean Atlas 2013 ver. 2

329 (https://www.nodc.noaa.gov/OC5/woa13/). The carbonate system variables (DIC and total

330 alkalinity) were determined from the Global Ocean Data Analysis Project version 2

331 (GLODAPv2, Olsen et al., 2016) and imposed as monthly climatology. The parameters and

332 biogeochemical coefficients used in ERSEM simulation were listed in Table 1.

333 **Table 1.** Variable definitions and values used in FVCOM-ERSEM coupling.

Symbol	Definition	Value			Unit
pCO2a	mole fraction of carbon dioxide in air	385			10^{-6}
a0w	adsorption coefficient of clear water	0.015			m^{-1}
b0w	backscatter coefficient of clear water	0.00135			m^{-2}
pEIR_eow	photosynthetically active fraction of shortwave radiation	0.5			-1
EPSESSa	specific shortwave absorption coefficient of silt	0.00004			$m^2\,mg^{-1}$
EPSESSb	specific shortwave backscatter coefficient of silt	0.00001			$m^2\,mg^{-1}$
N1p	initialization concentration of phosphate phosphorus	0.4			$mmol\,P\,m^{-3}$
N3n	initialization concentration of nitrate nitrogen	8			$mmol\,N\,m^{-3}$
N4n	initialization concentration of ammonium nitrogen	0.1			$mmol\,N\,m^{-3}$
N5s	initialization concentration of silicate	4.5			$mmol\,Si\,m^{-3}$
O2o	initialization concentration of oxygen	300			$mmol\,O_2\,m^{-3}$
O3c	total dissolved inorganic carbon	2130			$mmol\,C\,m^{-3}$
	Labile (R1), semi-labile (R2) and refractory (R3) dissolved organic carbon	**R1**	**R2**	**R3**	
c	initialization carbon concentration	10	12	12	$mg\,C\,m^{-3}$
n	initialization nitrogen concentration	0.14	-	-	$mmol\,N\,m^{-3}$

		R4	R6	R8	
p	initialization phosphorus concentration	0.01	-	-	mmol P m^{-3}
	Small (R4), medium (R6) and large (R8) particulate organic carbon	**R4**	**R6**	**R8**	
iopABS	specific shortwave absorption	0.00001	0.00001	0.00001	m^2 m^{-1} C
iopBBS	specific shortwave backscatter	0.000016	0.000016	0.000016	m^2 m^{-1} C
rm	sinking velocity	1	5	10	m d^{-1}
c	initialization carbon concentration	7.2	17	0.17	mg C m^{-3}
n	initialization nitrogen concentration	0.1	0.24	0.0024	mmol N m^{-3}
p	initialization phosphorus concentration	0.007	0.02	0.0002	mmol P m^{-3}
s	initialization silicate concentration	-	0.1	0.001	
	benthic dissolved (Q1), particulate (Q6) organic, refractory (Q7) matter	**Q1**	**Q6**	**Q7**	
remin	remineralisation rate	0.1	0.05	0.01	d^{-1}
pN3	nitrate fraction of remineralised nitrogen (remainder is ammonium)	0.9	0.9	0.9	Dimensionless
c	initialization carbon concentration	18.9	3052	30520	mg C m^{-2}
n	initialization nitrogen concentration	0.6	3.5	80	mg N m^{-2}
p	initialization phosphorus concentration	0.0035	0.5	8	mg P m^{-2}
resuspension	enable resuspension	TRUE	-	-	Dimensionless
vel_crit	critical shear velocity for resuspension	0.2	-	-	m s^{-1}
s	initialization silicate concentration	149	-	-	mg Si m^{-2}
pel_nitq10	q$_{10}$ temperature coefficient of pelagic nitrification	2			Dimensionless
pel_nitISWph	ph impact on pelagic nitrification (0:off,1:on)	1			Dimensionless
pel_nitsN4N3	specific nitrification rate of pelagic nitrification	0.5			1d^{-1}
pel_nitchN3o	michaelis-menten constant for cubic oxygen dependence of pelagic nitrification	2700			(mmol O2 m^{-3})^3
pel_nitchN4n	michaelis-menten constant for cubic ammonium dependence of pelagic nitrification	0.5			(mmol N m^{-3})^3
Ref_temp	reference temperature	10			degree C

		P1	P2	P3	P4	
	Diatoms (P1), Nanoflagellates (P2), Picoplankton (P3), and dinoflagellates (P4) phytoplankton functional groups	**P1**	**P2**	**P3**	**P4**	
sum	maximum specific productivity at reference temperature	1.375	1.625	2	1.125	1d^{-1}
q10	q10 temperature coefficient	2	2	2	2	Dimensionless
srs	specific rest respiration at reference temperature	0.04	0.04	0.045	0.035	1d^{-1}
pu_ea	excreted fraction of phytoplankton's primary production	0.2	0.2	0.2	0.2	Dimensionless
pu_ra	respired fraction of phytoplankton's primary production	0.2	0.2	0.2	0.2	Dimensionless
qnlc	minimum nitrogen to carbon ratio	0.0042	0.005	0.006	0.0042	mmol N mg^{-1} C
qplc	minimum phosphorus to carbon ratio	0.0001	0.000225	0.00035	0.0001	mmol P mg^{-1} C
xqcp	threshold for phosphorus limitation (relative to redfield ratio)	1	1	1	1	Dimensionless
xqcn	threshold for nitrogen limitation (relative to redfield ratio)	1	1	1	1	Dimensionless
xqp	maximum phosphorus to carbon ratio (relative to redfield ratio)	2	2	1.5	2.7	Dimensionless
xqn	maximum nitrogen to carbon ratio (relative to redfield ratio)	1.075	1.075	1.05	1.1	Dimensionless
qun3	nitrate affinity	0.0025	0.004	0.006	0.002	(m^3 mg^{-1} C)d^{-1}
qun4	ammonium affinity	0.0025	0.004	0.007	0.002	(m^3 mg^{-1} C)d^{-1}

qurp	phosphate affinity	0.003	0.004	0.006	0.002	$(m^3\ mg^{-1}\ C)d^{-1}$
snplux	specific tendency of luxury uptake of nutrients towards maximum quota	1	1	1	1	$1d^{-1}$
use_Si	if phytoplankton use silicate	TRUE	FALSE	FALSE	FALSE	Dimensionless
qsc	maximum silicate to carbon ratio	0.0118	-	-	-	$mmol\ Si\ mg^{-1}\ C$
chs	michaelis-menten constant for silicate limitation	0.2	-	-	-	$mmol\ m^{-3}$
sdo	1.1 of minimal specific lysis rate	0.05	0.05	0.055	0.045	$1d^{-1}$
alpha	initial slope of pi-curve	4	5	6	3	$((mg\ C\ m^2\ mg^{-1}\ Chl)\ W^{-1})d^{-1}$
beta	photoinhibition parameter	0.07	0.1	0.12	0.06	$((mg\ C\ m^2\ mg^{-1}\ Chl)\ W^{-1})d^{-1}$
phim	maximum effective chlorophyll to carbon photosynthesis ratio	0.06	0.025	0.015	0.045	$mg\ Chl\ mg^{-1}\ C$
uB1c_O2	oxygen produced per unit of carbon fixed	0.11	0.11	0.11	0.11	$mmol\ O_2\ mg^{-1}\ C$
urB1_O2	oxygen consumed per unit of carbon respired	0.1	0.1	0.1	0.1	$mmol\ O_2\ mg^{-1\ C}$
iopABS	specific shortwave absorption	0.007	0.0041	0.023	0.008	$m^2\ mg^{-1}\ Chl$
iopBBS	specific shortwave backscatter	0.00048	0.003	0.003	0.00048	$m^2\ mg^{-1}\ Chl$
resm	maximum nutrient-limitation-induced sinking velocity	5	0	0	5	$m\ d^{-1}$
c	initialization carbon concentration	8	5.9	5.9	5.9	$mg\ C\ m^{-3}$
n	initialization nitrogen concentration	0.1114	0.0926	0.0926	0.0926	$mmol\ N\ m^{-3}$
p	initialization phosphorus concentration	0.009	0.0036	0.0036	0.0036	$mmol\ P\ m^{-3}$
Chl	initialization chlorophyll a concentration	0.4	0.3	0.3	0.3	$mg\ m^{-3}$
P1s	initialization silicate concentration of diatoms	0.128				$mmol\ Si\ m^{-3}$
P2calcify	calcify of nanophytoplankton	TRUE				Dimensionless
L2sedL2	sinking velocity of calcite	10				$m\ d^{-1}$
L2c0	initialization carbon concentration of calcite	0.05				$mg\ C\ m^{-3}$
bL2remin	remineralisation rate of benthic calcite	0.05				$1d^{-1}$
bL2c	initialization carbon concentration of benthic calcite	0.05				$mg\ C\ m^{-2}$

Mesozooplankton (Z4), microzooplankton (Z5), nanoflagellates (Z6)		**Z4**	**Z5**	**Z6**	
q10	Q10 temperature coefficient	2	2	2	Dimensionless
minfood	Michaelis-Menten constant to perceive food	12	12	12	$mg\ C\ m^{-3}$
chuc	Michaelis-Menten constant for food uptake	36	32	28	$mg\ C\ m^{-3}$
sum	Maximum specific uptake at reference temperature	1	1.25	1.5	$1d^{-1}$
pu	Assimilation efficiency	0.6	0.5	0.4	Dimensionless
pu_ea	Fraction of unassimilated prey that is excreted (not respired)	0.5	0.5	0.5	Dimensionless
pe_R1	Dissolved fraction of excreted/dying matter	0.5	0.5	0.5	Dimensionless
srs	Specific rest respiration at reference temperature	0.015	0.02	0.025	$1d^{-1}$
sd	Basal mortality	0.05	0.05	0.05	$1d^{-1}$
sdo	Maximum mortality due to oxygen limitation	0.2	0.25	0.3	$1d^{-1}$
chro	Michaelis-Menten constant for oxygen limitation	7.81	7.81	7.81	Dimensionless
qpc	Phosphorus to carbon ratio	0.000786	0.001	0.001	$mmol\ P\ mg^{-1}\ C$
qnc	Nitrogen to carbon ratio	0.0126	0.0167	0.0167	$mmol\ N\ mg^{-1\ C}$
R1R2	Labile fraction of produced dissolved organic carbon	1	1	1	$1d^{-1}$
xR1p	Transfer of phosphorus to DOM, relative to POM	1.2	1.2	1.2	Dimensionless
xR1n	Transfer of nitrogen to DOM, relative to POM	1	1	1	Dimensionless

urB1_O2	Oxygen consumed per carbon respired	0.1	0.1	0.1	mmol O_2 mg^{-1} C
gutdiss	fraction of prey calcite that dissolves after ingestion	0.5	0.5	0.5	Dimensionless
c0	Background carbon concentration	0.0033	0.0033	0.0033	mg C m^{-3}
c	Initialization carbon concentration	1.2	7.2	2.421	mg C m^{-3}
Z4pu_eaR	Fraction of unassimilated detritus that is excreted (not respired)	0.9			Dimensionless
Z4Minprey	Food threshold for overwintering state of mesozooplankton	300			mg C m^{-2}
Z4repw	Specific overwintering respiration of mesozooplankton	0.0025			1d^{-1}
Z4mort	Specific overwintering mortality of mesozooplankton	0.0025			1d^{-1}
stempp	Specific excretion rate of excess phosphorus		0.5	0.5	1d^{-1}
stempn	Specific excretion rate of excess nitrogen		0.5	0.5	1d^{-1}
n	Initialization nitrogen concentration		0.12	0.0505	mmol N m^{-3}
p	Initialization phosphorus concentration		0.0113	0.047	mmol P m^{-3}
	bacteria	**B1**			
iswBlim	Nutrient limitation of bacteria (1:minimum of inorganic and organic availability,2:additive availability)	2			Dimensionless
q10	Q_{10} temperature coefficient of bacteria	2			Dimensionless
chdo	Michaelis-Menten constant for oxygen limitation of bacteria	0.31			Dimensionless
chn	Michaelis-Menten constant for nitrate limitation of bacteria	0.5			mmol N m^{-3}
chp	Michaelis-Menten constant for phosphate limitation of bacteria	0.1			mmol P m^{-3}
sd	Specific mortality of bacteria at reference temperature	0.05			1d^{-1}
sum	Maximum specific uptake of bacteria at reference temperature	2.2			1d^{-1}
pu	Efficiency of bacteria at high oxygen levels	0.6			Dimensionless
puo	Efficiency of bacteria at low oxygen levels	0.2			Dimensionless
srs	Specific rest respiration of bacteria at reference temperature	0.1			Dimensionless
sR1	Maximum turn-over rate of DOM of bacteria	1			1d^{-1}
qpc	Maximum phosphorus to carbon ratio of bacteria	0.0019			mmol P mg^{-1} C
qnc	Maximum nitrogen to carbon ratio of bacteria	0.0167			mmol N mg^{-1} C
ur_o2	Oxygen consumed per carbon respired of bacteria	0.1			mmol O_2 mg^{-1} C
sR1N1	Mineralisation rate of labile dissolved organic phosphorus of bacteria	0			1d^{-1}
sR1N4	Mineralisation rate of labile dissolved organic nitrogen of bacteria	0			1d^{-1}
fsink	Scavenging rate for iron of bacteria	0.00007			1d^{-1}
c0	Background carbon concentration of bacteria	0.01			mg C m^{-3}
rR2	Fraction of semi-labile DOC available to bacteria	0.0075			Dimensionless
rR3	Fraction of semi-refractory DOC available to bacteria	0.0025			Dimensionless
frR3	Fraction of activity respiration converted to semi-refractory DOC	0.3			Dimensionless
c	Initialization carbon concentration of bacteria	15.7			mg C m^{-3}
n	Initialization nitrogen concentration of bacteria	0.26			mmol N m^{-3}
p	Initialization phosphorus concentration of bacteria	0.029			mmol P m^{-3}

334

3.3 Univariate verification

336   To validate the model, the remote sensing data of *Chl-a* concentration from satellites
337 (MODIS-Aqua and GOCI) were used to perform model-data comparisons. Two sites located
338 offshore of the sediment plume were selected for this comparison (Fig. 3): site A (122.89°E,
339 31.46°N) and site B (122.80°E, 29.92°N). As shown in Fig. 4, the daily MODIS-Aqua *Chl_a* data
340 for 2005-2016 (red dots) were combined with the GOCI *Chl-a* data for 2012-2016 (blue dots)
341 and then used to verify the model-simulated *Chl-a* data (solid line). Two distinct blooms were
342 evident from the observational *Chl-a* in spring and in autumn, respectively. These blooms were
343 captured by the model-simulated results. The peaks of MODIS and simulated *Chl-a*
344 concentrations both reached ~ 10 mg/m^3 during the spring bloom. The root-mean-square-error
345 between them were 2.2 mg/m^3 and 2.47 mg/m^3 at Site A and B, respectively, indicating this
346 coupled model system successfully reproduced the magnitude and seasonal variations of *Chl-a* in
347 the offshore regions. Besides, the comparison between GOCI data and simulated *Chl-a* shown
348 that short-term temporal variations could also be captured by the model simulation. Although the
349 validation was conducted on a daily basis, it showed the variations over the time scale from
350 seconds to minutes as the model was integrated for iteration.
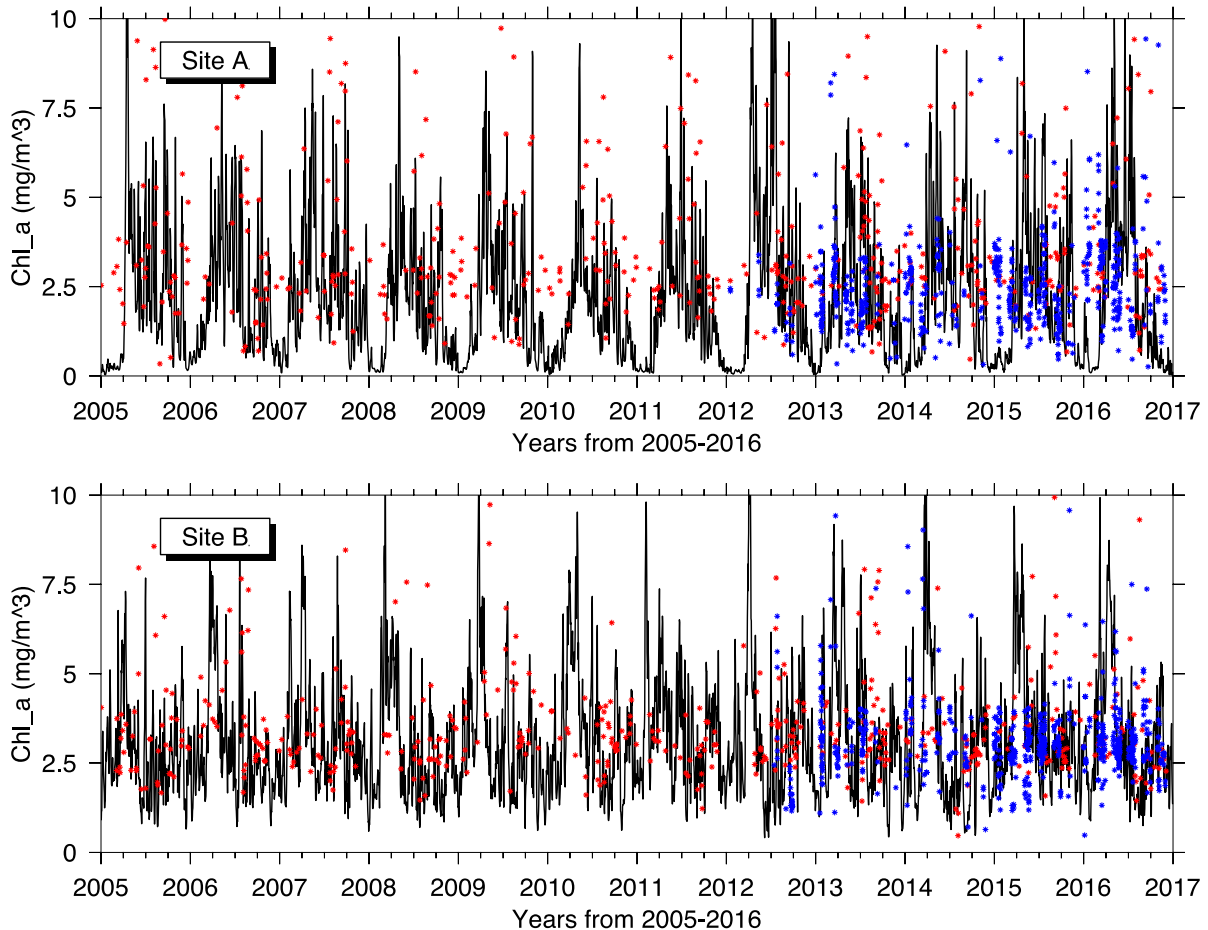
351

355   ## 3.3 Multivariate verification

356   In addition to useful independent and univariate assessments, the comparison between
357   model-simulated results and observations for all common variables simultaneously provides a
358   better evaluation of the overall performance of the model (Allen and Somerfield, 2009; Stow et
359   al., 2009). To determine the model's capability of revealing the realistic dynamics in the offshore
360   region, Principle Component Analysis (PCA) was applied to reduce the dimensionality of the
361   dataset and to identify the significant underlying components (Allen and Somerfield, 2009). PCA
362   was performed on both instantaneous observed values and daily averages of variables at
363   measurement sites from surface to bottom layers for salinity, temperature, *Chl-a*, SiO_3, NO_3,
364   PO_4, SPM, NH_4, and pH.

365   Both cumulative proportion of the first three eigenvectors of observed and simulated
366   variables were more than 90%, and the first two eigenvectors aggregated more than 85% (Table
367   2). This meant that the first principal component (PC1) and second principal component (PC2)
368   were able to reproduce the main factors that described the variability of the system as captured in
369   the observed variables. PC1 of observed and simulated variability accounted for 64.8% and
370   62.5%, respectively, both observed and simulated results indicated the very similar contribution
371   of salinity, temperature, SiO_3, NO_3 and PO_4. PC2 was 22.8% and 23.4%, respectively, with the
372   temperature to be the most essential. PC3 of the observed variability was mainly controlled by
373   the combination of NH_4 and suspended sediment, while that of model simulated variability was
374   under the mixed effect of NH4 and *Chl-a*.

375   **Table 2.** PCA Analysis of the modeling and measuring variables.

Eigenvector	observation			simulation		
	PC1	PC2	PC3	PC1	PC2	PC3
pH	-0.039	0.054	0.149	-0.361	-0.067	0.016
NH_4	-0.021	-0.070	0.891	-0.202	0.142	0.502
PO_4	0.402	-0.227	-0.046	0.273	-0.384	-0.231
NO_3	0.446	0.017	0.012	0.470	0.109	0.152
SiO_3	0.543	0.048	-0.093	0.462	0.148	0.139
Chl-a	0.006	0.149	0.058	-0.159	0.125	0.687
salinity	-0.581	-0.167	-0.116	-0.495	-0.283	-0.159
temperature	-0.035	0.935	0.070	-0.153	0.835	-0.391
SPM	0.059	-0.116	0.389	0.160	-0.020	0.039
variance	0.65	0.23	0.04	0.62	0.23	0.07
variance%	64.89	22.84	3.75	62.49	23.46	7.28
cumulative%	64.89	87.73	91.48	62.49	85.94	93.23

376   The ordination values in the PCA demonstrated the similarity between the main modes of
377   variability in both observed and modeled variables, and the seasonal changes associated with the
378   controls on the pelagic ecosystem and environmental conditions (Fig. 5). The samples of the two
379   datasets in summer were in the positive direction of PC2 axis and the samples in winter were in
380   the negative direction of PC2 axis because of the dominating control of temperature in PC2. The

381 observation PCA points had a more compact distribution than the simulated results. This implied
382 that the model reproduced the observed variability to some degree. The high positive values on
383 PC2 axis were possibly related with the overestimation of river temperature. In general, both
384 patterns from PCA showed some similarities, indicating the model revealed the major modes of
385 seasonal effects of the biogeochemical variables, at least on winter/summer seasons.

386
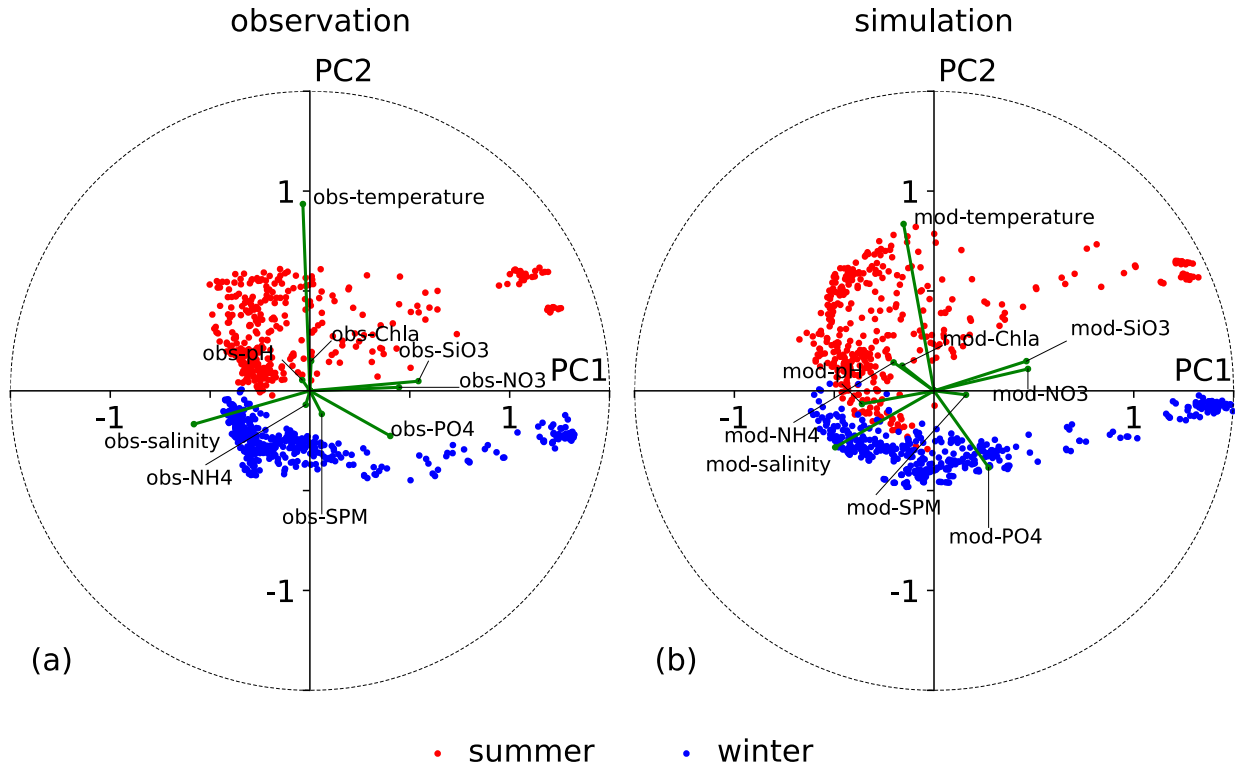
Figure 5. Principle Component Analyses (PCA) based on observed (a) and simulated (b) *Chl-a*, nitrate, silicate,
phosphate and ammonia concentrations as well as temperatures, salinities, pH levels and SPM values. The simulated
values were the nearest equivalent to the measurements in temporal and spatial coordinates. Data were normalized
before the analysis was performed. PC1 and PC2 indicate the first and second principal components, respectively.

4. Nutrient and phytoplankton simulations

4.1 *Chl-a* and sediment front

To determine the seasonal variability of phytoplankton under the condition with
sediments, we calculated the seasonal means of surface *Chl-a* overlapped with the sediment
concentration (Fig. 6). Four seasons were defined as follow, March-May as spring, June-August
as summer, September-November as autumn and December-February as winter. At this level of
aggregation, the model results clearly showed two distinct zones separated by the waters with
high-concentration suspended sediment and with high phytoplankton *Chl-a* concentration,
respectively. The computational domain contained several significant high-turbidity zones,
including the Changjiang Estuary, Hangzhou Bay and the coastal region off Jiangsu Province.
The model also reproduced the seasonal variation of sediment dynamics in the offshore regions
of the Changjiang Estuary and Jiangsu. The sediment front in the Changjiang Estuary was
confined within 122.5°E during spring and summer (Fig. 6a-b), but extended to 123°E in autumn

and winter (Fig. 6c-d). In the Jiangsu offshore region, there was a similar pattern, but with further offshore extension in autumn and winter, which reached ~124.3°E in winter.
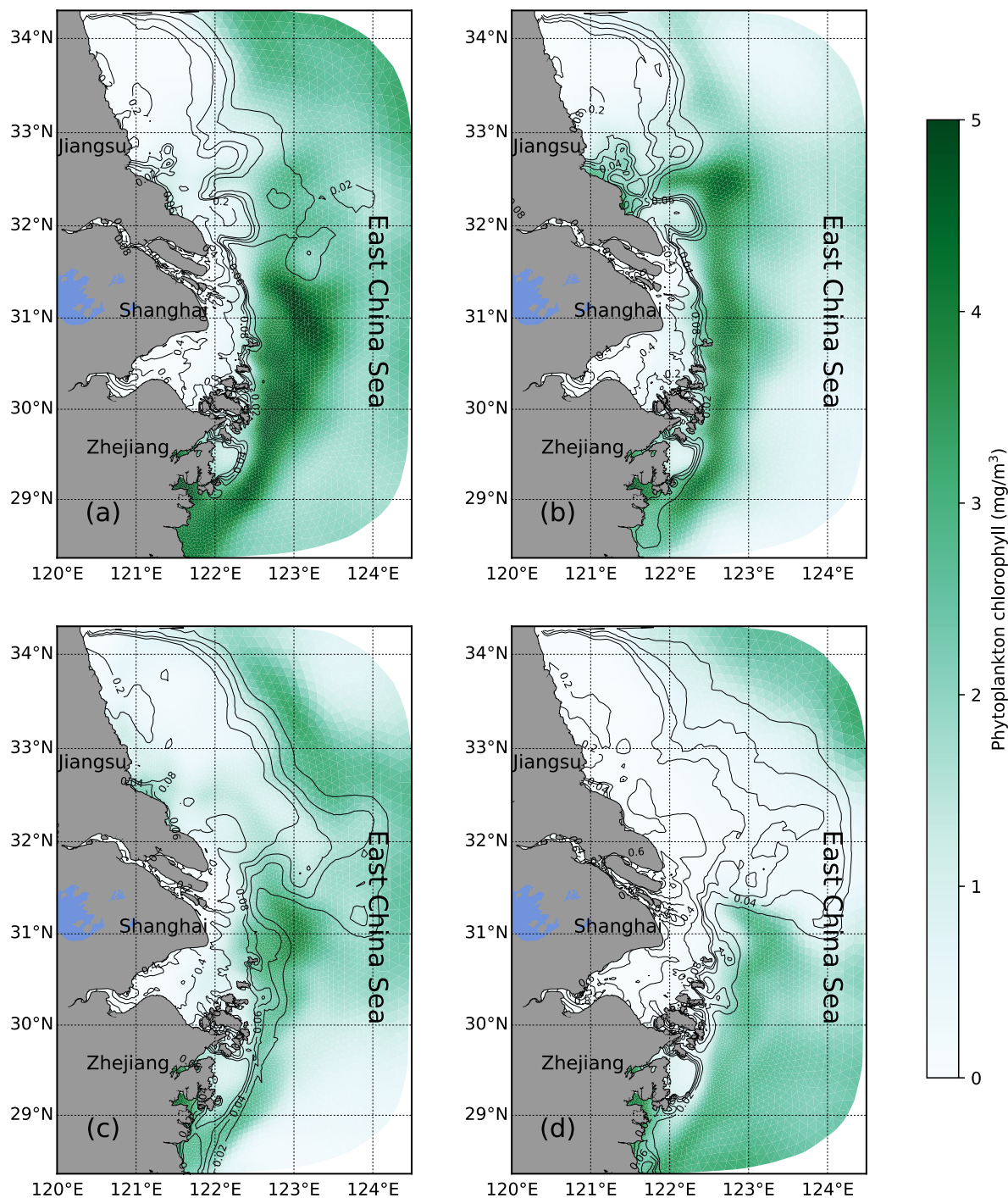
Figure 6. Seasonal-averaged surface distributions of the suspended sediment concentration (contour, unit: g/L) and phytoplankton *Chl-a* concentration (colored image, unit: mg/m³) during spring (a), summer (b), autumn (c) and winter (d).

However, the extension of this sediment front is not uniquely controlled by the remote horizontal sediment advection. Local resuspension dynamics in combination with vertical

412 stratification were responsible for the behavior and extension of the sediment plume. In spring
413 and summer, in the offshore region, under strong stratification condition, it was due to the off-
414 shore extension of the low-salinity river plume (Wu et al., 2011; Ge et al., 2015). The advection
415 of riverine derived SSC was the major driving force since the ambient concentrations were low.
416 Surface heating in these two seasons also played an important role in intensifying stratification.
417 This limited the upward vertical transport of sediment in the offshore region and led to low SSC
418 in the upper water column. With sufficient nutrient supply, the increase in light availability in the
419 surface layers under a low SSC condition made a more favor environment for the phytoplankton
420 growth in the offshore region compared to the nearshore and estuarine region.

421 In autumn and winter, the physical conditions changed. Due to decreasing freshwater
422 discharge and colder weather-induced surface cooling, the offshore destratification occurred.
423 Vertical mixing increased the local resuspension of sediment throughout the water column (Luo
424 et al., 2018), producing the high broad-scale sediment concentration at the surface (Fig. 6d).
425 Under lower water temperature and light penetration, the phytoplankton growth in the offshore
426 region was greatly limited.

427 4.2 Diatom and non-diatom phytoplankton group

428 Multiple species of phytoplankton jointly contributed to the total *Chl-a* concentration in
429 the observations and model results. In the shelf of the ECS, diatoms and dinoflagellates are the
430 major groups and generally represent up to 90 % of the total biomass in the spring bloom (Chen
431 et al., 2003; Zhu et al., 2009). While the single specie *Skeletonema costatum* dominates the
432 diatom group, dinoflagellates are represented by hundreds of species, covering sizes from
433 microphytoplankton (> 20 μm), nanophytoplankton (2–20 μm), to picophytoplankton (< 2 μm).
434 Nonetheless, the dominant specie is *Prorocentrum donghaiense*. In order to facilitate the
435 comparison with observations and known dynamics in the region, we have aggregated the model
436 results for microphytoplankton, nanophytoplankton and picophytoplankton from FVCOM-
437 ERSEM modeling results as a non-diatom phytoplankton group.

438 To determine the major phytoplankton group that contributes to the increase of *Chl-a* in
439 spring and summer (Fig. 6a-b), the surface carbon-based (not *Chl-a*-based) biomass of diatom
440 and non-diatom phytoplankton were shown in Fig. 7. The overall diatom percentage in the
441 phytoplankton community was about 43% during spring. The results showed that diatom carbon
442 distribution (Fig. 7a) matched well with the pattern of the *Chl-a* concentration during spring
443 season (Fig. 6a), indicating the diatom had a major contribution to the *Chl-a* concentration.
444 However, the diatom biomass was weaker than the non-diatom group, including dinoflagellate
445 and other small-size species. The distribution pattern of diatom followed the *Chl-a* distribution,
446 which were confined offshore but closed to the sediment frontal boundary along the estuary,
447 indicating light availability limits the diatom growth. Non-diatom biomass was higher offshore
448 of the sediment front in the shelf region, particularly in the northeastern region, where the non-
449 diatom concentration reached 200 mg C/m^3, while the *Chl-a* concentration remained low (50-75
450 mg C/m^3) in spring due to nutrient limitation.

451 In summer, the diatom percentage in total biomass of phytoplankton declined to 37%，
452 especially on the offshore side of the sediment front (Fig. 7c). The wide diatom biomass regions
453 shrank to a narrow band along the sediment front on the offshore side with a maximum
454 concentration declining from ~175 to ~80 mg C/m^3, resulting from the diatoms' dependency on
455 light and nutrient physiologically. On the other hand, non-diatom had high biomass both along

18

456　the sediment front and even in the out region, with a maximum concentration of more than 200
457　mg C/m³ (Fig. 7d).
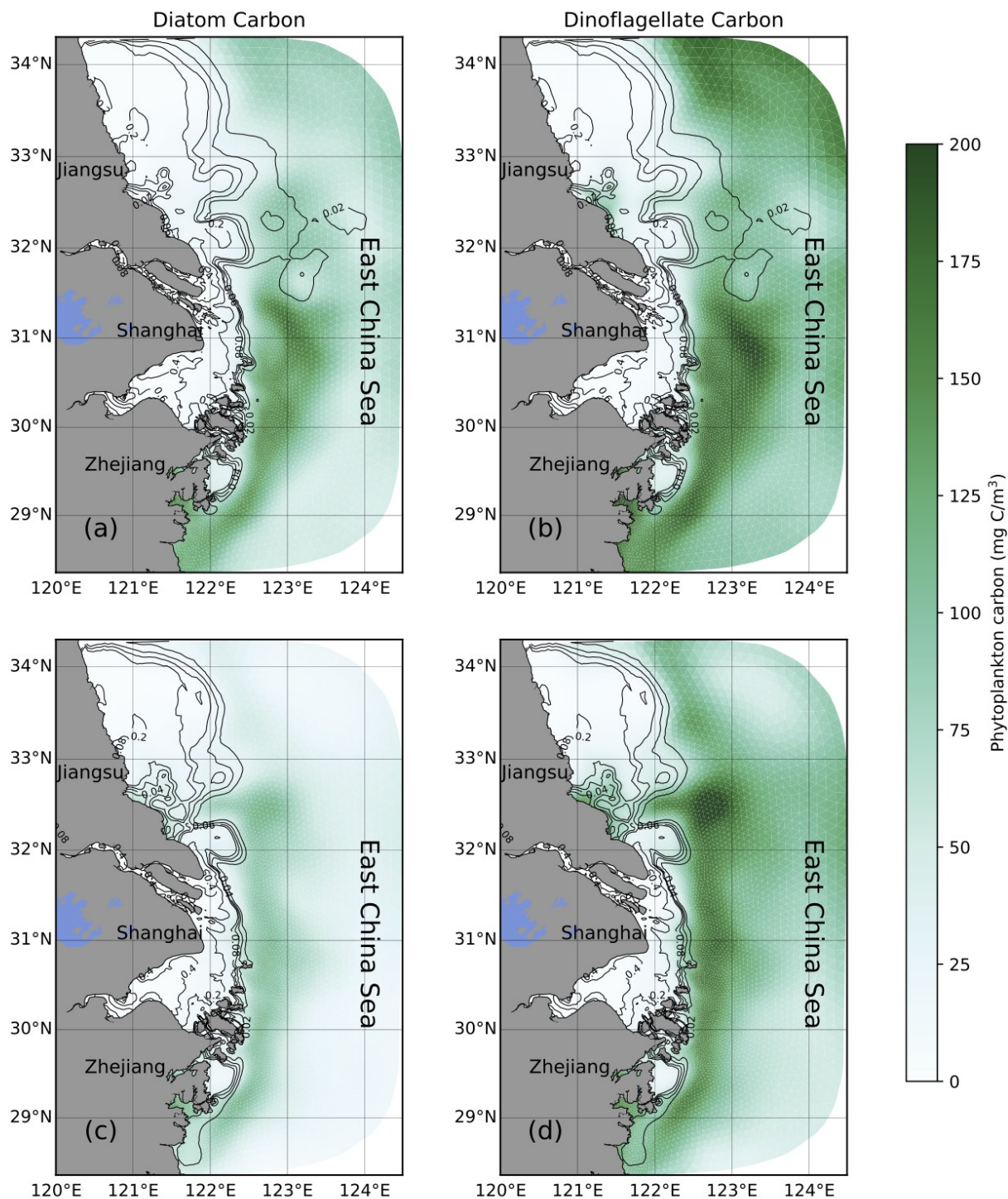
459 **Figure 7.** Seasonal-averaged surface distributions of the suspended sediment concentration (unit: g/L) (contours)
460 and biomass (colored image; unit: mg C/m^3) of diatom (a, c) and dinoflagellate (b, d) (colored image) during spring
461 (a-b) and summer (c-d).

462

463 4.3 Dissolved Nutrients

464 Taking the nitrogen flux from the Changjiang Estuary for example, the annual DIN flux
465 was about 1.25×10^{11} mol yr^{-1}; the particulate nitrogen, however, was only about 0.9×10^{10} mol
466 yr^{-1} (Gao et al., 2012). The content of PN was less than 10% of total nitrogen. The particulate
467 nutrient was only a small component in the whole nutrient based on the measurements in the
468 Changjiang River (Gao et al., 2012). Among the various phosphorus forms, particulate
469 phosphorus represented <50%, and is closely related to the concentration of suspended sediment
470 concentration (Liu et al., 2016). Nonetheless, the dissolved inorganic nutrients made the major
471 contribution to the phytoplankton growth and ecosystem cycle. Therefore, the temporal and
472 spatial variabilities of nutrients were determined through their dissolved inorganic forms.

473 While dissolved nutrients were mainly dominated by the Changjiang River source in the
474 study area, they experienced various seasonal behaviors. Taking the DIN and DIP as examples,
475 they behaved conservatively in the high-turbidity area, undergoing only physical dilution from
476 the river channel to the river mouth (Fig. 8-9). Phytoplankton growth was quite weak in this area,
477 and thus no significant nitrate was consumed. In the offshore region, DIN was consumed in the
478 offshore side region of the sediment front during spring and summer (Fig. 8a-b), causing a sharp
479 decrease over there. However, since the DIN was not the limiting factor in this system, the
480 concentrations in the offshore region of the sediment front were still high, 40-70 mmol N/m^3 in
481 summer (Fig. 8b) and 10-30 mmol N/m^3 in winter (Fig. 8d). With the eastward extension of the
482 sediment front in autumn and winter, the DIN reached the offshore region as a result of
483 advection (Fig. 8c-d).

484 DIP, on the other hand, was the limiting dissolved nutrient in the ecosystem of the
485 Changjiang Estuary and adjacent regions (Gao et al., 2005; Zhou et al., 2017). In addition to
486 riverine sources, local mixing, pelagic and benthic bacterial mediated degradation were also the
487 significant sources of DIP, causing DIP varying with the stratification status. DIP produced by
488 these dynamics had the similar distribution patterns as the surface sediment. Phytoplankton
489 growth consumed most of DIP in the water column during spring, summer and autumn, forming
490 the same boundary of DIP and SSC at the sea surface in these three seasons (Fig. 9a-c). Outside
491 the sediment front, the concentration of DIP was quite low, indicating DIP was depleted due to
492 the growth of phytoplankton. In winter, the concentration of DIP increased in the offshore area
493 due to vertical mixing and weak growth of phytoplankton (Fig. 9d), and similar behavior was
494 seen in DIN in the offshore area (Fig. 8d). In winter, vertical mixing provided more dissolved
495 nutrients to the upper column (Fig. 8d and Fig. 9d) and supported the growth of phytoplankton
496 offshore in Zhejiang, where the suspended sediment concentration was relatively low.
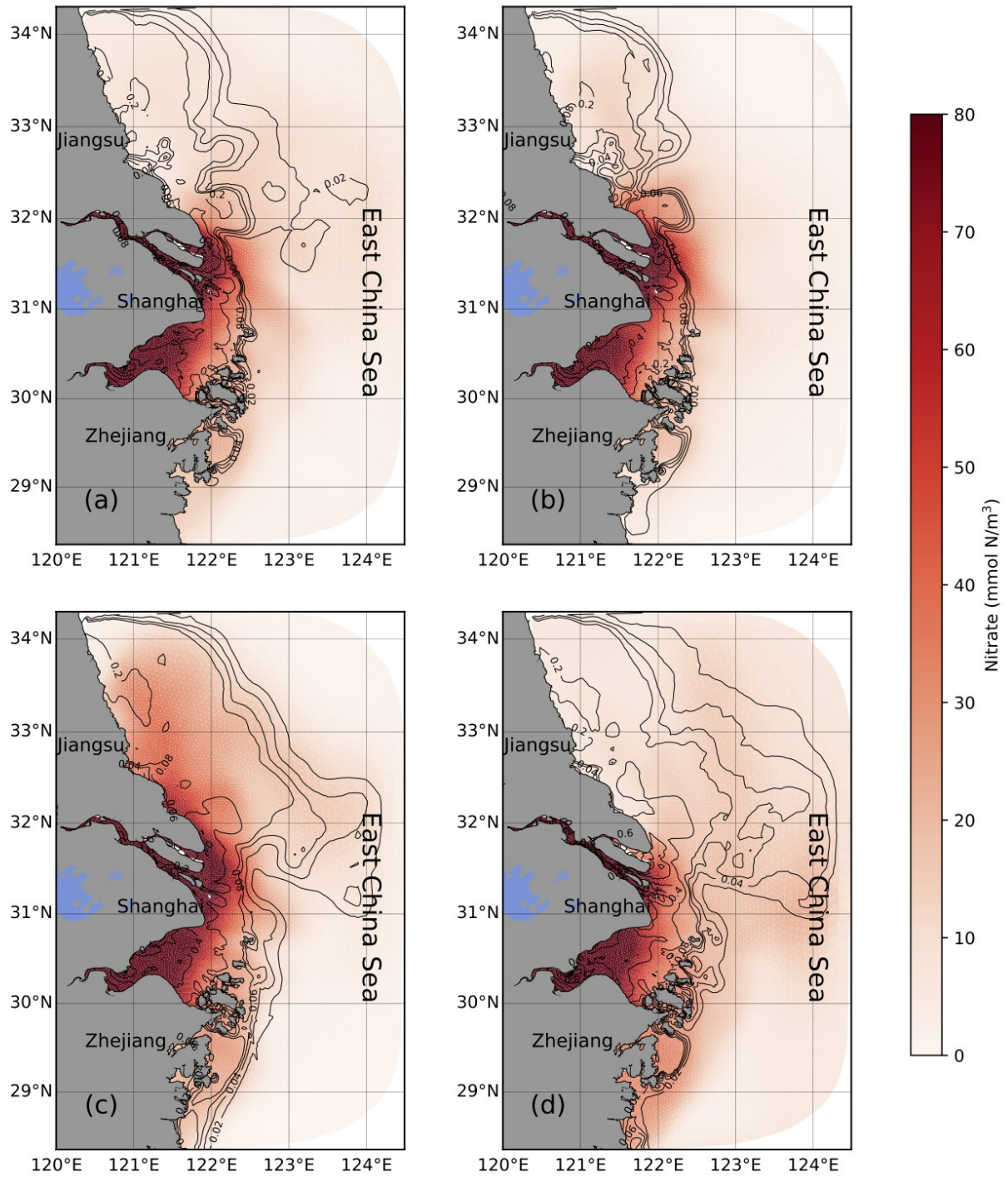
Figure 8. Seasonal-averaged surface distributions of suspended sediment concentration (contour, unit: g/L) and DIN (colored image, unit: mmol N/m^3) during spring (a), summer (b), autumn (c) and winter (d).
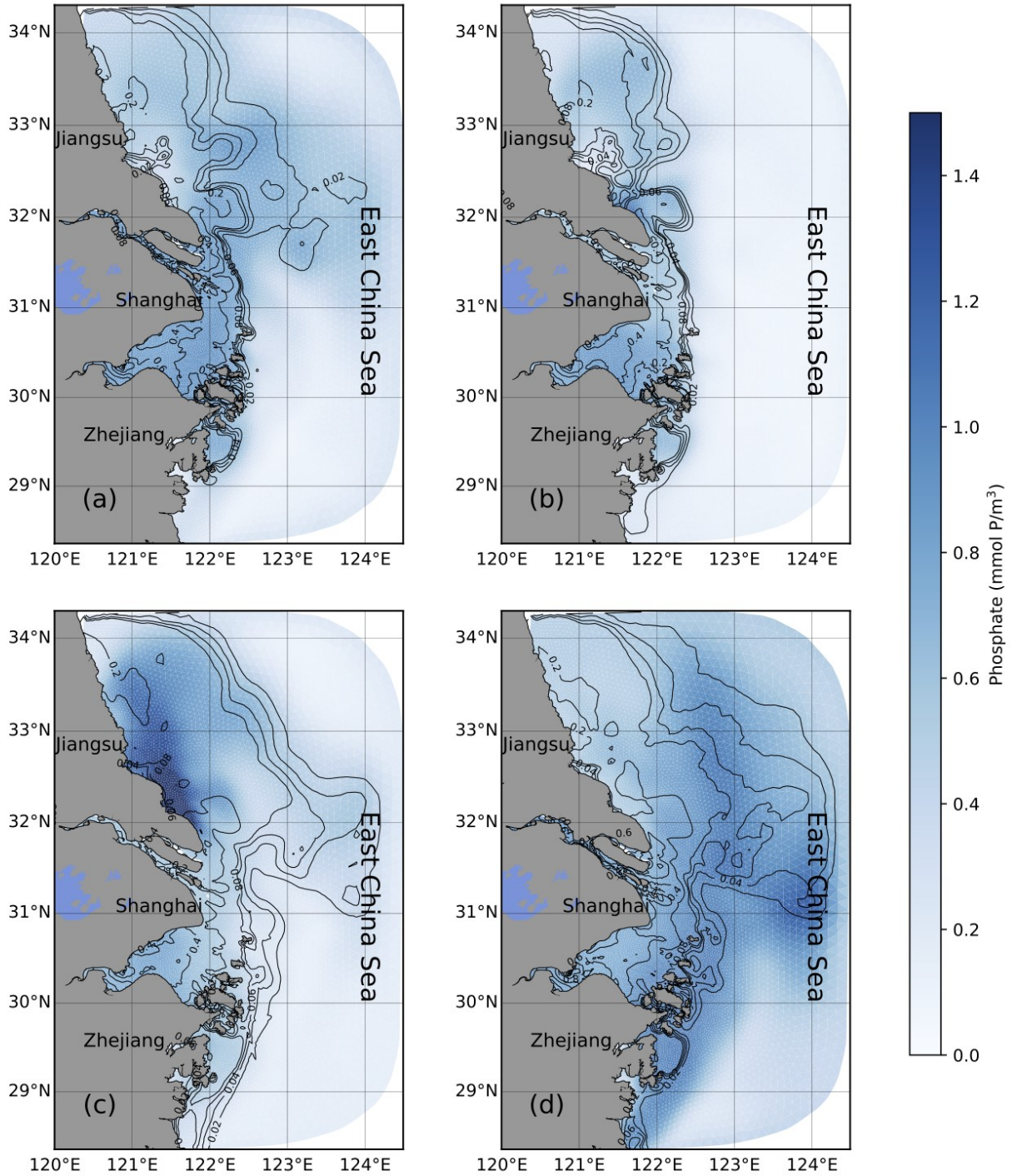
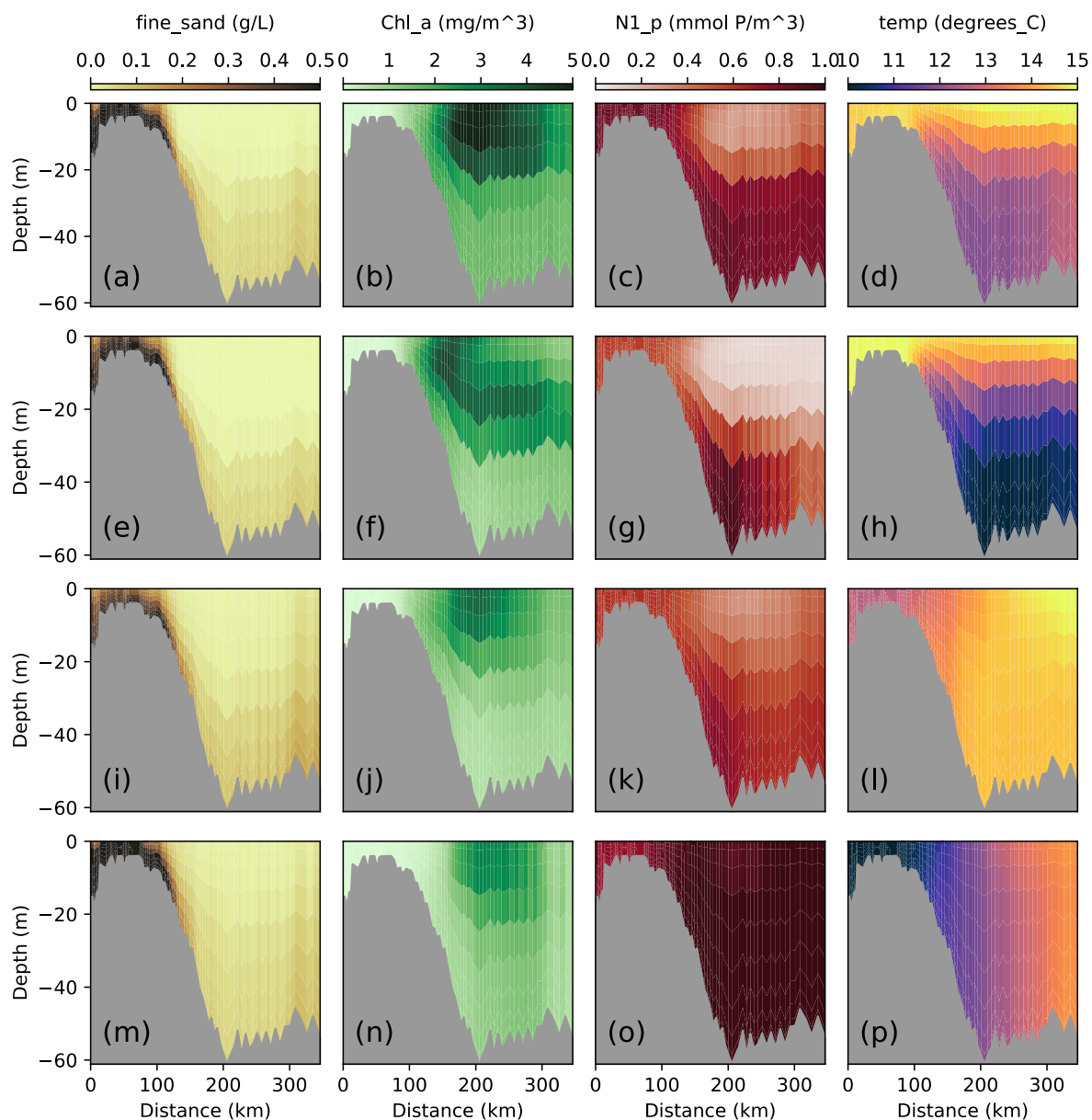**Figure 9.** Seasonal-averaged surface distributions of suspended sediment concentration (contour, unit: g/L) and DIP (colored image, unit: mmol P/m^3) during spring (a), summer (b), autumn (c) and winter (d).

Vertical mixing in the offshore region played an important role in the seasonal regulation of sediment, phytoplankton and dissolved nutrients as mentioned above. Thus, a vertical section from the river mouth to the offshore region was selected to investigate the seasonal variability of the vertical distribution (blue dashed line in Fig. 3). On this transect, the SSC in the upper layer

507 of the offshore region increased from summer to winter (Fig.10e, i and m) due to the decrease in
508 stratification and higher resuspension driven by the increasing vertical mixing (Fig. 10h, l and p).
509 The highest concentration of *Chl-a* in the low-turbidity upper column represented the spring
510 bloom of phytoplankton (Fig. 10b). The DIP distribution showed a distinct low-value zone due to
511 the consumption by phytoplankton in the upper column (Fig. 10c).

512   In summer, the stratification was strongest (Fig. 10h), resulting in the lowest sediment
513 concentrations in the upper water column (Fig. 10e). Under this weak-mixing condition, the DIP
514 in the upper column was depleted after the spring bloom and not replenished via vertical mixing
515 (Fig. 10g), this dissolved nutrient limiting decreased the phytoplankton growth at the surface.
516 Under these conditions, a subsurface *Chl-a* maximum developed (Fig. 10f).

517
518 **Figure 10.** Seasonal-averaged vertical distributions of the suspended sediment concentration (first column, unit:
519 g/L), phytoplankton (second column, unit: mg/m³), DIP (third column, unit: mmol P/m³), and temperature (forth
520 column, unit: degree) on the selected section during spring (a-d), summer (e-h), autumn (i-l) and winter (m-p).

23

521   With stronger vertical mixing from autumn to winter, and additional remineralization of
522 detritus from dead phytoplankton, zooplankton and other biological components, the
523 concentration of DIP reached its peak in winter. The whole water column became well mixed
524 with DIP concentrations reaching ~0.8 mmol P/m^3.

525   In summary, the interactions between the physical and biogeochemical processes
526 modulated the seasonal variabilities of dissolved nutrients and phytoplankton around the offshore
527 area. The sediment dynamics confined the light penetration in the water column, which
528 dominated the boundary of phytoplankton growth. Vertical mixing in the different seasons led to
529 different dissolved nutrient supplies regimes, with river supplies becoming less important in
530 autumn and winter.

531   Although dissolved nutrients were the major components of nutrient states, it should be
532 noted that besides the dissolved form, the particulate nutrients, both organic and inorganic form,
533 also contributed to the nutrient cycle, especially for the phosphorus (Liu et al., 2016). The
534 particulate nutrients had much more complex dynamics, such as interaction with suspended
535 sediment particles. Since most of available measurements for nutrients in this study were based
536 on dissolved form, the only dynamics of dissolved nutrients were examined. The particulate
537 nutrients should be resolved if one needs to understand full dynamics of nutrients on all forms.

538

539 **5. Discussion**

540   5.1 Interpretation from remote sensing data

541   Remote sensing from satellite platforms has been recognized as a useful method to
542 retrieve surface SPM and *Chl-a* (O'Reilly et al., 1998; Shen et al., 2010). Using the semi-
543 empirical radiative transfer (SERT) algorithm with physical based empirical coefficients (Shen et
544 al., 2010), the snapshot for the Changjiang Estuary and its adjacent regions at 07:16 am May 16,
545 2016 in the spring season illustrated the offshore extent of the SSC in Fig. 11a. It appeared that
546 turbid water covered the whole coastal region with the typical sediment concentration of ~500
547 mg/L. In the offshore region, the concentrations declined to 20-50 mg/L, where light penetrated
548 into the water column and promote phytoplankton growth.

549   *Chl-a* was mostly observed in the offshore region (Fig. 11b), where relatively low-
550 turbidity water presented (Fig 11a). In the turbidity maximum and coastal high-turbidity regions,
551 the concentration of *Chl-a* was low due to light limitation. The front between the high-, and low-
552 turbidity water acted like a boundary for phytoplankton growth, which demonstrated the
553 sediment's modulation of phytoplankton dynamics. The location of modeled high *Chl-a* in spring
554 matched the spot where historical spring bloom was observed (Gao et al., 2005; Zhu et al., 2009;
555 Guo et al., 2014). The distribution of *Chl-a* concentration showed a narrow band off the
556 sediment front in May.

557   The snapshots of SPM and *Chl-a* from remote sensing also revealed the existence of
558 small-scale structures along the sediment front. These fine structures suggested the existence of
559 eddies along the low-salinity front. Chen et al. (2008) proposed that such eddies were produced
560 by baroclinic instabilities due to the salinity-induced density gradient. These eddies also led to
561 some isolated patches of high-turbidity water, causing detachment occurred, then resulting in the
562 horizontal mixing of coastal high-turbidity water and offshore low-turbidity water. it was

partially responsible for the supply of dissolved nutrients that supported that narrow diatom patch along the front. The snapshot from remote sensing showed that sediment-phytoplankton interactions exhibited much more complicated temporal and spatial variations on tidal or wind-event scales. This was a mechanism presented in the model and it was responsible for the supply of dissolved nutrients that supported that narrow diatom patch along the front over a short time scale. This eddy-induced water exchange between inner and outer regions of the front was revealed also in previous studies (Chen et al., 2008; Ge et al., 2015a). However, it should be noted that these structures have been smoothened during the temporally-averaging on the seasonal scale shown in Fig. 6-9.
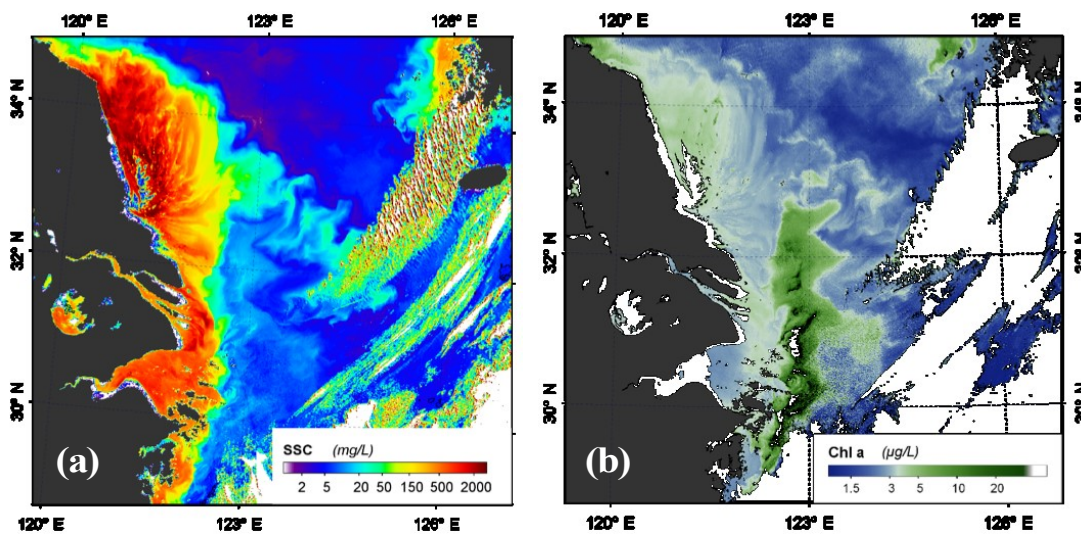

Figure 11. Distributions of the GOCI-retrieved surface sediment concentration (a) and *Chl-a* (b) around the Changjiang Estuary from the snapshot at 15:30PM, May 16th, 2016.

5.2 Influence of ocean circulation

Besides the regulation effect that riverine sediment or locally resuspended sediment had on phytoplankton and nutrient dynamics, the oceanic flow also played an important role in the offshore dynamics of the pelagic ecosystem. The Taiwan Warm Current (TWC) is the strongest oceanic intrusion in the offshore region of the Changjiang Estuary, influencing the physical and biogeochemical conditions.

In summer, the TWC reached the Changjiang Estuary, with seasonal-averaged velocities of ~0.1m/s in the bottom layer (~40-50m) (Fig. 12a). This current carried high-temperature water from the south to the north. Additionally, the intrusion of TWC and Kuroshio were recognized as a water mass with relatively higher DIP concentration in the bottom column, compared with adjacent shelf water (Chen et al., 2003b, Zhou et al., 2017). These higher-DIP water from intrusion and its induced upwelling partly supported the dinoflagellate bloom in the coastal region (Zhou et al., 2019). Along the selected dashed line in Fig. 12a, the SSC was relatively low, less than 10 mg/L in the offshore area (Fig. 12b), indicating the SPM had s weak effect on the biogeochemical process in this area. While there was low DIP concentration of less than 0.1 mmol/m^3 in the surface water, the TWC contributed to higher DIP in bottom (> 0.6 mmol/m^3), thus vertically stratified DIP distribution was seen from Fig. 12c with additive effect from summer stratification in water column discussed in Section 4. Due to low SPM, the light reached

593 subsurface layer (~25-30m), and enabled the development of a subsurface *Chl-a* maximum
594 where the nutrients were adequate for phytoplankton growth (Fig. 12c), which matches well with
595 previous measurements in Chen et al. (2003b). Previous observations also indicated that the DIP
596 from the TWC played a critical role in the maintenance of dinoflagellate blooms here (Zhou et
597 al., 2017).
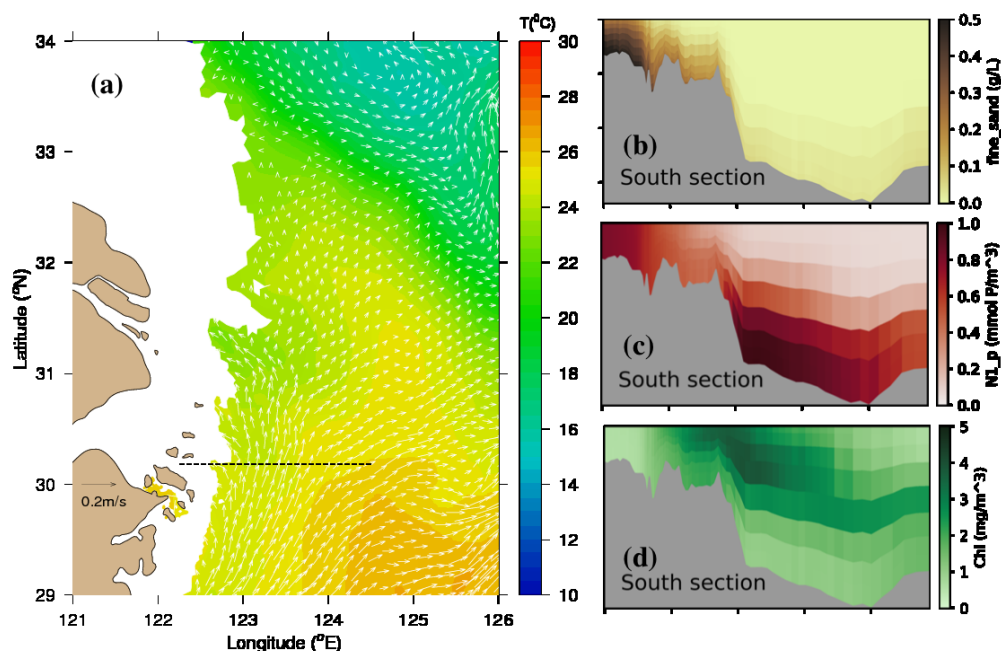
598

599 **Figure 12.** Seasonal-averaged flow vectors and temperature at 40-m depth (a) in summer. Vertical distribution of
600 SPM (b), phosphate (c) and *Chl-a* (d) along the dashed-line section shown in (a).

601   5.3 Zooplankton impact

602   Phytoplankton biomass are not the only functional groups depending on nutrients and
603 light. There are four phytoplankton, three zooplankton and one bacteria functional groups in
604 ERSEM model, so the competition (for resources, i.e. nutrients) and predation also plays a role.
605 Low summer diatoms biomass generally reflects both higher predation pressure from
606 zooplankton and competition from smaller phytoplankton and bacteria which have higher growth
607 rates and smaller sedimentation rates. In fact, zooplankton predation together with nutrient
608 depletion contributes to the demise of the diatom spring bloom.

609   The model results showed that the total zooplankton biomass (mesozooplankton,
610 microzooplankton and heterotrophic flagellates) on the seasonal scale mainly followed the
611 distribution of phytoplankton, namely higher concentrations during spring and summer, and
612 lower concentrations in autumn and winter (Fig. 13). Zooplankton dominated the larger offshore
613 areas of the sediment front, reaching the outer shelf where non-diatom biomass was adequate to
614 be predated. Meanwhile, low zooplankton concentration (<70 mg C/m^3) was found within the
615 coastal region in all seasons.
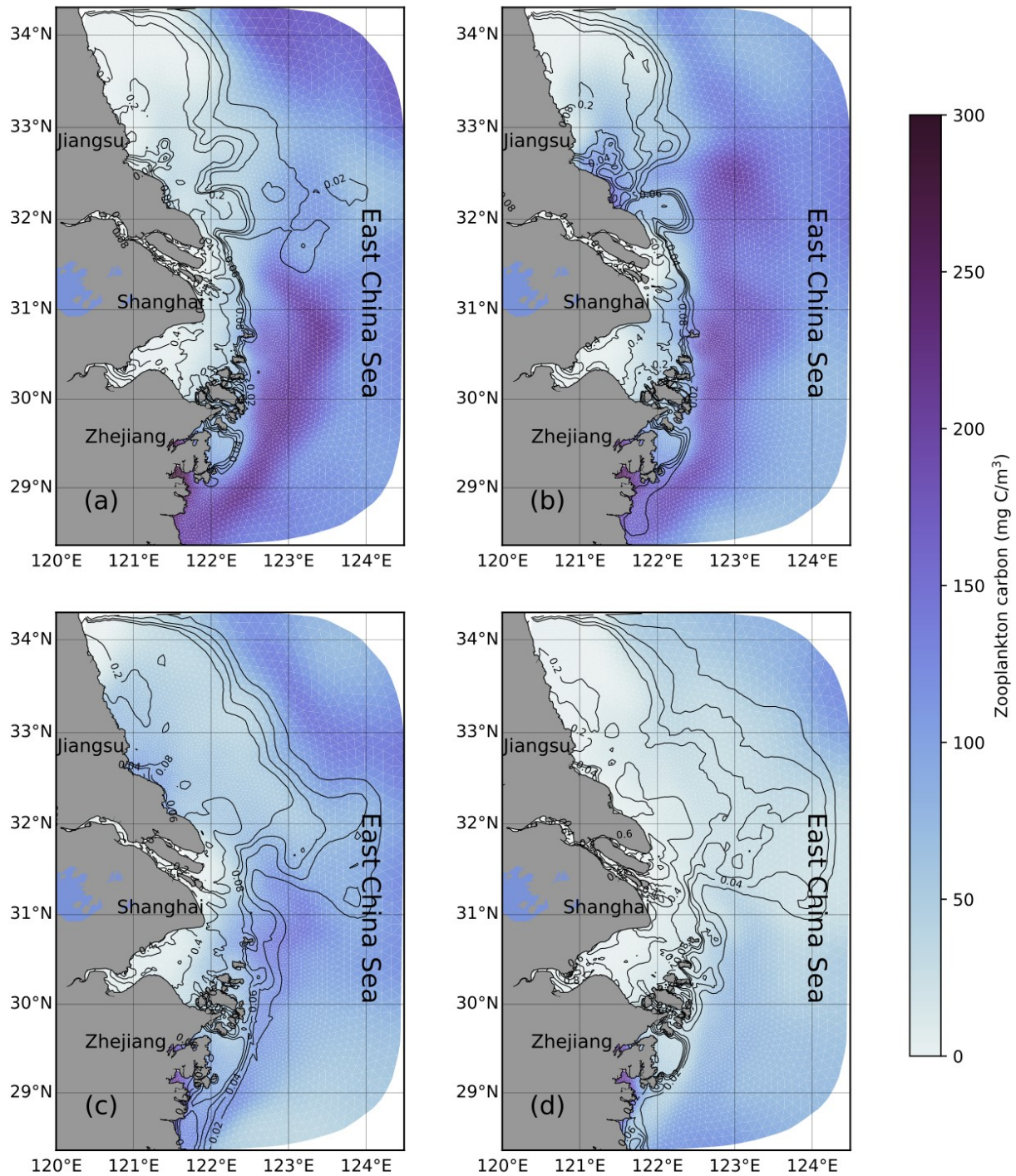
Figure 13. Seasonal-averaged surface distributions of the suspended sediment concentration (contour) and total biomass of zooplankton (colored image) during spring (a), summer (b), autumn (c) and winter (d).

5.4 Stability of seasonal structures

The model simulation covered the time period from 1999 to 2016. Besides the atmospheric and oceanic variabilities that caused the model fluctuations, the major influencing factor for the Changjiang Estuary and adjacent region could be the construction of the Three Gorges Dam. It became operational in 2003, and caused very strong sedimentation impact on the lower reach of the Changjiang river. The sediment concentration into the estuary has significant decreased, as well as the annual sediment load (Luan et al., 2016; Yang et al., 2015). However, the decrease in sediment concentration mainly occurred in the river channel from Datong station to river mouth. The offshore region, particularly around the sediment front region in this study, did not show significant variation trend based on continuous remote sensing from 2003 to 2010 (Shen et al., 2013). It mainly indicated a local temporal oscillation. The annual freshwater flux before and after the construction of the Three Gorges Dam were of the same amplitude (Luan et al., 2016).

Since the freshwater discharge and offshore sediment concentration did not change significantly, the seasonality of dissolved nutrients and phytoplankton has remained relatively stable before and after the operation of Three Gorges Dam. The magnitude of nutrient and phytoplankton concentration surely has some oscillation, which probably was still caused by increasing use of fertilizers.

5.5 Stoichiometry in sediment and nutrients

Nutrients entering the estuarine environment, with an additional contribution from submarine groundwater discharges, can undergo rapid adsorption into suspended sediments with the potential to conversely have desorption processes during transportation and resuspension, or even deposit into sea bed (Wang et al., 2018; Liu et al., 2017, 2018). It should be noted that the absorption and desorption of nutrients in the suspended particulate matters were not included in the ERSEM. Nutrients were treated as dissolved and particulate states in the biogeochemical model. Based on previous experiments, the nitrate has weak capacity on absorption and desorption in sediment, whereas the phosphate has notable absorption and desorption processes with suspended sediment. In future studies, the sediment's biogeochemical process should be included in whole nutrient cycle, particularly the adsorption/desorption behavior for phosphorus, given its great importance in high-turbidity environments such as the Changjiang Estuary and adjacent coastal regions.

6. Summary

In this study, a coupled physical-biogeochemical model system, based on FVCOM and ERSEM, was developed to examine the impact of the sediment front on the nutrients and phytoplankton dynamics over the inner shelf of the ECS off the high-turbidity Changjiang Estuary. The model system successfully revealed the variation of *Chl-a* in the offshore region, reproducing the major variability modes of various physical and biogeochemical variables obtained from the seasonal field campaigns as seen in PCA. The model results revealed that the suspended sediments played a role in regulating the growth of phytoplankton. Influenced by the seasonal variations in the extension of low-salinity water, which carried nutrients and sediment, the phytoplankton followed the sediment front from more onshore locations during spring and summer to further offshore locations during autumn and winter. Results demonstrated that diatoms were major contributors to *Chl-a* concentration, but lower biomass contribution to total

663 phytoplankton carbon, and non-diatoms (i.e. dinoflagellates etc.) dominated out of the sediment
664 front, and extended to the outer shelf region.

665   DIN and DIP had different behaviors on the seasonal scale. Nitrate behavior could
666 generally be approximated by physical dilution and transport of freshwater discharge, and
667 remained high offshore of the sediment front. Whereas phosphate, acting as the limiting nutrient
668 in the ecosystem, showed more local dynamics and reached lower concentrations offshore of the
669 front. It's implied from the vertical profiles that vertical mixing largely controlled sediment re-
670 suspension, nutrient mixing and phytoplankton distribution in the offshore water column.
671

681

References

683 Allen, J. I., & Somerfield, P. J. (2009). A multivariate approach to model skill assessment.
684   *Journal of Marine Systems*, 76(1), 83–94. http://doi.org/10.1016/j.jmarsys.2008.05.009

685 Baretta-Bekker, J. G., Baretta, J. W., & Koch Rasmussen, E. (1995). The microbial food web in
686   the European Regional Seas Ecosystem Model. *Netherlands Journal of Sea Research*,
687   33(3-4), 363–379. http://doi.org/10.1016/0077-7579(95)90053-5

688 Beardsley, R. C., Chen, C., & Xu, Q. (2013). Coastal flooding in Scituate (MA): A FVCOM
689   study of the 27 December 2010 nor'easter. *Journal of Geophysical Research-Oceans*,
690   118(11), 6030–6045. http://doi.org/10.1002/jgrc.20443

691 Blackford, J. C., Allen, J. I., & Gilbert, F. J. (2004). Ecosystem dynamics at six contrasting sites:
692   a generic modelling study. *Journal of Marine Systems*, 52(1-4), 191–215.
693   http://doi.org/10.1016/j.jmarsys.2004.02.004

694 Boynton, W. R., Ceballos, M. A. C., Bailey, E. M., Hodgkins, C. L. S., Humphrey, J. L., &
695   Testa, J. M. (2018). Oxygen and Nutrient Exchanges at the Sediment-Water Interface: a
696   Global Synthesis and Critique of Estuarine and Coastal Data. *Estuaries and Coasts*,
697   41(2), 1–33. http://doi.org/10.1007/s12237-017-0275-5

698 Bruggeman, J., & Bolding, K. (2014). A general framework for aquatic biogeochemical models.
699   *Environmental Modelling and Software*, 61(C), 249–265.
700   http://doi.org/10.1016/j.envsoft.2014.04.002

701 Butenschon, M., Clark, J., Aldridge, J. N., Allen, J. I., Artioli, Y., Blackford, J., et al. (2016).
702   ERSEM 15.06: a generic model for marine biogeochemistry and the ecosystem dynamics
703   of the lower trophic levels. *Geoscientific Model Development*, 9(4), 1293–1339.
704   http://doi.org/10.5194/gmd-9-1293-2016-supplement

705 Cazenave, P. W. and Bedington, M. (2018). PyFVCOM (version 2.1.3) [software]. Plymouth,
706   Devon, United Kingdom: Plymouth Marine Laboratory.
707   https://doi.org/10.5281/zenodo.1422462

708 Chen, C., Beardsley, R. C., and Limeburner, R. (1994). Comparison of winter and summer
709   hydrographic observations in the Yellow and East China Seas and adjacent Kuroshio
710   during 1986. *Continental Shelf Research*. 14, 909-929.

Chen, C. H. Liu, R. C. Beardsley. (2003a). An unstructured, finite-volume, three-dimensional, primitive equation ocean model: application to coastal ocean and estuaries. *Journal of Atmospheric and Oceanic Technology*. 20, 159-186.

Chen, C., J. Zhu, R. C. Beardsley, and P. S. Franks. (2003b). Physical-Biological Sources for the Dense Algal Bloom over the Western Shelf of the East China Sea. *Geophysical Research Letter*. 30(10), 1515, 22-1:4.

Chen, C., L. Wang, R. Ji, J. W. Budd, D. J. Schwab, D. Beletsky, G. L. Fahnenstiel, H. A. Vanderploeg, B. J. Eadie, and J. Cotner (2004). Impacts of suspended sediment on the ecosystem in Lake Michigan: A comparison between the 1998 and 1999 plume events. *Journal of Geophysical Research*. 109(C10S05):18,

Chen, C, R. C. Beardsley and G. Cowles (2006). An unstructured grid, finite-volume coastal ocean model (FVCOM) system. Special Issue entitled "Advance in Computational Oceanography", *Oceanography*. vol. 19, No. 1, 78-89.

Chen, C. P. Xue, P. Ding, R. C. Beardsley, Q.Xu, X. Mao, G. Gao, J. Qi, C. Li, H. Lin, G. Cowles and M. Shi (2008). Physical mechanisms for the offshore detachment of the Chanjiang diluted water in the East China Sea. *J. Geophys. Res*., 113. C02002, doi: 10.1029/2006JC003994.

Chen, C., R.C. Beardsley, G. Cowles, J. Qi, Z. Lai, G. Gao, D. Stuebe, Q. Xu, P. Xue, J. Ge, R. Ji, S. Hu, R. Tian, H. Huang, L. Wu, H. Lin, Y. Sun and L. Zhao (2013), An unstructured grid, finite-volume community ocean model FVCOM user manual, SMAST/UMASSD Technical Report 13-0701, School of Marine Science and Technology, University of Massachusetts-Dartmouth, New Bedford, MA, USA

Choi, J. K., Y. J. Park, J. H. Ahn, H. S. Lim, J. Eom, and J. H. Ryu (2012), GOCI, the world's first geostationary ocean color observation satellite, for the monitoring of temporal variability in coastal water turbidity, *J. Geophys. Res*., 117, C09004, doi:10.1029/2012JC008046.

Choi, J. K., J. E. Min, J. H. Noh, T. H. Han, S. Yoon, Y. J. Park, J. E. Moon, J. H. Ahn, S. M. Ahn, and J. H. Park (2014), Harmful algal bloom (HAB) in the East Sea identified by the Geostationary Ocean Color Imager (GOCI), *Harmful Algae*, 39, 295-302,

CWRC (Changjiang Water Resources Commission) (2011). Changjiang Sediment Bulletin. available at:. http://www.cjh.com.cn/pages/nsgb.html (in Chinese).

Donohue, I., & Garcia Molinos, J. (2009). Impacts of increased sediment loads on the ecology of lakes. *Biological Reviews*, 84(4), 517–531. http://doi.org/10.1111/j.1469-185X.2009.00081.x

de Swart, H. E., Schuttelaars, H. M., & Talke, S. A. (2009). Initial growth of phytoplankton in turbid estuaries: A simple model. *Continental Shelf Research*, 29(1), 136–147. http://doi.org/10.1016/j.csr.2007.09.006

Ebenhoh, W., Kohlmeier, C., Radford, P.J. (1995). The benthic bio-logical model in the European Regional Seas Ecosystem Model. *Netherlands Journal of Sea Research*, 33, 423–452.

Egbert, G. D., & Erofeeva, S. Y. (2002). Efficient inverse modeling of barotropic ocean tides. *Journal of Atmospheric and Oceanic Technology*, 19(2), 183–204.

Friedl, G. & Wüest, A. (2002). Disrupting biogeochemical cycles - Consequences of damming *Aquat. sci*. 64: 55. https://doi.org/10.1007/s00027-002-8054-0

Furuya, K., Kurita, K., and Odate, T. (1996). Distribution of phytoplankton in the East China Sea in the winter of 1993, *J. Oceanogr*., 52, 323–333, https://doi.org/10.1007/BF02235927,

Furuya, K., Hayashi, M., Yabushita, Y., and Ishikawa, A. (2003). Phytoplankton dynamics in the East China Sea in spring and summer as revealed by HPLC-derived pigment signatures, *Deep-Sea Res. Pt. II*, 50, 367–387, https://doi.org/10.1016/S0967-0645(02)00460-5.

Gao, X., & Song, J. (2005). Phytoplankton distributions and their relationship with the environment in the Changjiang Estuary, China. *Marine Pollution Bulletin*, 50(3), 327–335. http://doi.org/10.1016/j.marpolbul.2004.11.004

Ge, J., Ding, P., Chen, C., Hu, S., Fu, G., & Wu, L. (2013). An integrated East China Sea–Changjiang Estuary model system with aim at resolving multi-scale regional–shelf–estuarine dynamics. *Ocean Dynamics*, 63(8), 881–900. http://doi.org/10.1007/s10236-013-0631-3

Ge, J., Chen, C., & Ding, P. (2015). Estimation of critical shear stress for erosion in the Changjiang Estuary: A synergy research of observation, GOCI sensing and modeling. *Journal of Geophysical Research-Oceans*, 120(1), 8439–8465. http://doi.org/10.1002/2015JC010992

Ge, J., Ding, P., & Chen, C. (2015). Low-salinity plume detachment under non-uniform summer wind off the Changjiang Estuary. *Estuarine, Coastal and Shelf Science*, 156(C), 61–70. http://doi.org/10.1016/j.ecss.2014.10.012

Ge, J., Zhou, Z., Yang, W., Ding, P., Chen, C., Wang, Z. B., & Gu, J. (2018). Formation of Concentrated Benthic Suspension in a Time-Dependent Salt Wedge Estuary. *Journal of Geophysical Research-Oceans*, 123(11), 8581–8607. http://doi.org/10.1029/2018JC013876

Geider R.J., MacIntyre H.L., Kana T.M. (1997). A dynamic model of phytoplankton growth and acclimation: responses of the balanced growth rate and the chlorophyll a:carbon ratio to light, nutrient-limitation and temperature. *Mar Ecol Prog Ser* 148:187-200

Guo, S., Feng, Y., Wang, L., Dai, M., Liu, Z., Bai, Y., & Sun, J. (2014). Seasonal variation in the phytoplankton community of a continental-shelf sea: the East China Sea. *Marine Ecology Progress Series*, 516, 103–126. http://doi.org/10.3354/meps10952

He, Q., Qiu, Y., Liu, H., Sun, X., Kang, L., Cao, L., et al. (2017). New insights into the impacts of suspended particulate matter on phytoplankton density in a tributary of the Three Gorges Reservoir, China. *Scientific Reports*, 7(1), 1–11. http://doi.org/10.1038/s41598-017-13235-0

Hu, B., Wang, P., Zhang, N., Wang, C., & Ao, Y. (2016). Photoproduction of dissolved organic carbon and inorganic nutrients from resuspended lake sediments. *Environmental Science and Pollution Research*, 23(21), 1–10. http://doi.org/10.1007/s11356-016-7327-4

Huettel, M., Berg, P., & Kostka, J. E. (2014). Benthic Exchange and Biogeochemical Cycling in Permeable Sediments. *Annual Review of Marine Science*, 6(1), 23–51. http://doi.org/10.1146/annurev-marine-051413-012706

794 Jiang T, Yu ZM, Song XX, Cao XH, Yuan YQ. (2010). Long-term ecological interactions
795   between nutrient and phytoplankton community in the Changjiang estuary. *Chin J*
796   *Oceanol Limnol*; 28: 887–98.

797 Jiang, Z., Chen, J., Zhou, F., Shou, L., Chen, Q., Tao, B., et al. (2015). Controlling factors of
798   summer phytoplankton community in the Changjiang (Yangtze River) Estuary and
799   adjacent East China Sea shelf. *Continental Shelf Research*, 101, 1–14.
800   http://doi.org/10.1016/j.csr.2015.04.009

801 Ji, R., C. Chen, J. Budd, D. Schwab, D. Beletsky, D. Fahanenstial, T. H. Johengen, H.
802   Lavrentyev, B. Eadies, J. Cotner, W. Gardner and M. Bundy (2002). A coupled
803   biological and physical model study of the ecosystem in Lake Michigan Part II: Influence
804   of suspended sediment. *Ecological Modeling*. 152, 169-190.

805 Klausmeier C.A., Litchman E., Daufresne T. and Levin S. (2008). Phytoplankton stoichiometry.
806   *Ecol. Res.*, 23, 479–485.

807 Lamquin, N., C. Mazeran, D. Doxaran, J. H. Ryu, and Y. J. Park (2012), Assessment of GOCI
808   radiometric products using MERIS, MODIS and field measurements, *Ocean Science*
809   *Journal*, 47(3), 287-311

810 Liu, S.-M., Qi, X. H., Li, X., Ye, H. R., Wu, Y., Ren, J. L., et al. (2016). Nutrient dynamics from
811   the Changjiang (Yangtze River) estuary to the East China Sea. *Journal of Marine*
812   *Systems*, 154(Part A), 15–27. http://doi.org/10.1016/j.jmarsys.2015.05.010

813 Luan, H. L., Ding, P.-X., Wang, Z. B., Ge, J.-Z., & Yang, S.-L. (2016). Decadal morphological
814   evolution of the Yangtze Estuary in response to river input changes and estuarine
815   engineering projects. *Geomorphology*, 265(C), 12–23.
816   http://doi.org/10.1016/j.geomorph.2016.04.022

817 Luo, Z., Zhu, J., Wu, H., & Li, X. (2017). Dynamics of the sediment plume over the Yangtze
818   Bank in the Yellow and East China Seas. *Journal of Geophysical Research: Oceans*, 122,
819   10,073– 10,090. https://doi.org/10.1002/2017JC013215

820 Niemistö, J., Kononets, M., Ekeroth, N., Tallberg, P., Tengberg, A., & Hall, P. O. J. (2018).
821   Benthic fluxes of oxygen and inorganic nutrients in the archipelago of Gulf of Finland,
822   Baltic Sea – Effects of sediment resuspension measured in situ. *Journal of Sea Research*,
823   135, 95–106. http://doi.org/10.1016/j.seares.2018.02.006

824 Qi, J., Chen, C., Beardsley, R., Perrie, W., Cowles, G., & Lai, Z. (2009). An unstructured-grid
825   finite-volume surface wave model (FVCOM-SWAVE): Implementation, validations and
826   applications. *Ocean Modelling*, 28(1-3), 153–166.

827 Qi, J., Chen, C., & Beardsley, R. C. (2018). FVCOM one-way and two-way nesting using
828   ESMF_ Development and validation. *Ocean Modelling*, 124, 94–110.
829   http://doi.org/10.1016/j.ocemod.2018.02.007

830 Olsen, A., Key, R. M., van Heuven, S., Lauvset, S. K., Velo, A., Lin, X., et al. (2016). The
831   Global Ocean Data Analysis Project version 2 (GLODAPv2) – an internally consistent
832   data product for the world ocean. *Earth System Science Data*, 8(2), 297–323.
833   http://doi.org/10.5194/essd-8-297-2016

834   Piwowarczyk, L., H. Bishop, K. Saia, S. Crosby, F. T. Mudymba, N. I. Hashi, and A. Raj (2016),
835   Application of GOCI Satellite Data to Ocean Modeling, *J. Coastal Res.*, 15(1), 1409-
836   1414,

837   Ryu, J.-H., Han, H.-J., Cho, S., Park, Y.-J., & Ahn, Y.-H. (2012). Overview of geostationary
838   ocean color imager (GOCI) and GOCI data processing system (GDPS). *Ocean Science*
839   *Journal*, 47(3), 223–233. http://doi.org/10.1007/s12601-012-0024-4

840   Sadat-Noori, M., Santos, I. R., Tait, D. R., & Maher, D. T. (2016). Fresh meteoric versus
841   recirculated saline groundwater nutrient inputs into a subtropical estuary. *Science of the*
842   *Total Environment*, the, 566-567(C), 1440–1453.
843   http://doi.org/10.1016/j.scitotenv.2016.06.008

844   Shen, F., W. Verhoef, Y. Zhou, M. S. Salama, and X. Liu (2010), Satellite Estimates of Wide-
845   Range Suspended Sediment Concentrations in Changjiang (Yangtze) Estuary Using
846   MERIS Data, *Estuar. Coast.*, 33(6), 1420-1429, doi:10.1007/s12237-010-9313-2

847   Shen, F., Zhou, Y., Li, J., He, Q., & Verhoef, W. (2013). Remotely sensed variability of the
848   suspended sediment concentration and its response to decreased river discharge in the
849   Yangtze estuary and adjacent coast. *Continental Shelf Research*, 69(C), 52–61.
850   http://doi.org/10.1016/j.csr.2013.09.002

851   Stow, C. A., Jolliff, J., McGillicuddy, D. J., Jr., Doney, S. C., Allen, J. I., Friedrichs, M. A. M.,
852   et al. (2009). Skill assessment for coupled biological/physical models of marine systems.
853   Journal of Marine Systems, 76(1-2), 4–15. http://doi.org/10.1016/j.jmarsys.2008.03.011

854   Sun, X., F. Shen, D. Liu, R. G. Bellerby, Y. Liu, and R. Tang (2018), In Situ and Satellite
855   Observations of Phytoplankton Size Classes in the Entire Continental Shelf Sea, China, *J.*
856   *Geophys. Res. Oceans*, 123(5), 3523-3544,

857   Siswanto, E., Tang, J., Yamaguchi, H., Ahn, Y.-H., Ishizaka, J., Yoo, S., et al. (2011). Empirical
858   ocean-color algorithms to retrieve chlorophyll-a, total suspended matter, and colored
859   dissolved organic matter absorption coefficient in the Yellow and East China Seas.
860   *Journal of Oceanography*, 67(5), 627–650. http://doi.org/10.1007/s10872-011-0062-z

861   Sokoletsky, L., Yang, X., & Shen, F. (2014). MODIS-based retrieval of suspended sediment
862   concentration and diffuse attenuation coefficient in Chinese estuarine and coastal waters.
863   In R. J. Frouin, D. Pan, & H. Murakami (Eds.), (Vol. 9261, p. 926119). Presented at the
864   SPIE Asia Pacific Remote Sensing, SPIE. http://doi.org/10.1117/12.2069205

865   O'Reilly, J. E., S. Maritorena, B. G. Mitchell, D. A. Siegel, K. L. Carder, S. A. Garver, M.
866   Kahru, and C. McClain, (1998). Ocean color chlorophyll algorithm for SeaWiFS. *Journal*
867   *of Geophysical Research*, 103(C11): 24937-24953.

868   Olsen A, Key RM, van Heuven S, Lauvset SK, Velo A, Lin X, Schirnick C, Kozyr A, Tanhua T,
869   Hoppema M, Jutterstro ̈m S, Steinfeldt R, Jeansson E, Ishii M, Pe ́rez FF, Suzuki T
870   (2016). The Global Ocean Data Analysis Project version 2 (GLODAPv2)—aninternally
871   consistent data product for the world ocean. *Earth Syst Sci Data* 8:297–323.
872   https://doi.org/10.5194/essd-8-297-2016

873   Moore, W. S. (2010). The Effect of Submarine Groundwater Discharge on the Ocean. *Annual*
874   *Review of Marine Science*, 2(1), 59–88. http://doi.org/10.1146/annurev-marine-120308-
875   081019

Moore, W.S., J.O. Blanton, S. Joye (2006). Estimates of Flushing Times, Submarine Groundwater Discharge, and Nutrient Fluxes to Okatee River, South Carolina, *J. Geophys. Res*., 111, C09006, doi:10.1029/2005JC003041,.

Moore, W.S. (2006). The role of submarine groundwater discharge in coastal biogeochemistry. *Journal of Geochemical Exploration*, 88, 389-393,.

Hu, C., L. Feng, and Z. P. Lee (2012), Evaluation of GOCI sensitivity for At-Sensor radiance and GDPS-Retrieved chlorophyll-a products, *Ocean Science Journal*, 47(3), 279-285,

Li, M., Xu, K., Watanabe, M., & Chen, Z. (2007). Long-term variations in dissolved silicate, nitrogen, and phosphorus flux from the Yangtze River into the East China Sea and impacts on estuarine ecosystem. *Estuarine, Coastal and Shelf Science*, 71(1-2), 3–12. http://doi.org/10.1016/j.ecss.2006.08.013

Liu, J., Su, N., Wang, X., & Du, J. (2017). Submarine groundwater discharge and associated nutrient fluxes into the Southern Yellow Sea: A case study for semi-enclosed and oligotrophic seas-implication for green tide bloom. *Journal of Geophysical Research-Oceans*, 122(1), 139–152. http://doi.org/10.1002/2016JC012282

Liu, J., Du, J., Wu, Y., & Liu, S. (2018). Nutrient input through submarine groundwater discharge in two major Chinese estuaries: the Pearl River Estuary and the Changjiang River Estuary. *Estuarine, Coastal and Shelf Science*, 203, 17–28. http://doi.org/10.1016/j.ecss.2018.02.005

Vanderploeg, H. A., Johengen, T. H., Lavrentyev, P. J., Chen, C., Lang, G. A., Agy, M. A., et al. (2007). Anatomy of the recurrent coastal sediment plume in Lake Michigan and its impacts on light climate, nutrients, and plankton. *Journal of Geophysical Research*, 112(C3), C03S90. http://doi.org/10.1029/2004JC002379

Wang, X., Baskaran, M., Su, K., & Du, J. (2018). The important role of submarine groundwater discharge (SGD) to derive nutrient fluxes into River dominated Ocean Margins – The East China Sea. *Marine Chemistry*, 204, 121–132. http://doi.org/10.1016/j.marchem.2018.05.010

Wang, Y., Wu, H., Gao, L., Shen, F., & Liang, X. S. (2019). Spatial Distribution and Physical Controls of the Spring Algal Blooming Off the Changjiang River Estuary. *Estuaries and Coasts*, 42(4), 1–18. http://doi.org/10.1007/s12237-019-00545-x

Wu, L., Chen, C., Guo, P., Shi, M., Qi, J., & Ge, J. (2011). A FVCOM-based unstructured grid wave, current, sediment transport model, I. Model description and validation. *Journal of Ocean University of China*, 10(1), 1–8. http://doi.org/10.1007/s11802-011-1788-3

Wu, H., Zhu, J., Shen, J., & Wang, H. (2011). Tidal modulation on the Changjiang River plume in summer. *Journal of Geophysical Research*, 116(C8), C08017. http://doi.org/10.1029/2011JC007209

Yang, S. L., Xu, K. H., Milliman, J. D., Yang, H. F., & Wu, C. S. (2015). Decline of Yangtze River water and sediment discharge: Impact from natural and anthropogenic changes. *Scientific Reports*, 1–14. http://doi.org/10.1038/srep12581

Zhu, Z.-Y., Ng, W.-M., Liu, S.-M., Zhang, J., Chen, J.-C., & Wu, Y. (2009). Estuarine phytoplankton dynamics and shift of limiting factors: A study in the Changjiang (Yangtze

917   River) Estuary and adjacent area. *Estuarine, Coastal and Shelf Science*, 84(3), 393–401.
918   http://doi.org/10.1016/j.ecss.2009.07.005

919 Zhu, Z.-Y., Wu, Y., Zhang, J., Du, J.-Z., & Zhang, G.-S. (2014). Reconstruction of
920   anthropogenic eutrophication in the region off the Changjiang Estuary and central Yellow
921   Sea_ From decades to centuries. *Continental Shelf Research*, 72(C), 152–162.
922   http://doi.org/10.1016/j.csr.2013.10.018

923 Zhou, M.-J., Shen, Z.-L., & Yu, R.-C. (2008). Responses of a coastal phytoplankton community
924   to increased nutrient input from the Changjiang (Yangtze) River. *Continental Shelf*
925   *Research*, 28(12), 1483–1489. http://doi.org/10.1016/j.csr.2007.02.009

926 Zhou, Y., Zhang, Y., Li, F., Tan, L., & Wang, J. (2017). Nutrients structure changes impact the
927   competition and succession between diatom and dinoflagellate in the East China Sea.
928   *Science of the Total Environment*, the, 574(C), 499–508.
929   http://doi.org/10.1016/j.scitotenv.2016.09.092

930 Zhou, Z.-X., Yu, R.-C., Sun, C., Feng, M., & Zhou, M.-J. (2019). Impacts of Changjiang River
931   Discharge and Kuroshio Intrusion on the Diatom and Dinoflagellate Blooms in the East
932   China Sea. *Journal of Geophysical Research-Oceans*, 8(1), 39–14.
933   http://doi.org/10.1029/2019JC015158

934